JACS
JOURNAL OF THE AMERICAN CHEMICAL SOCIETY

ARTICLE

pubs.acs.org/JACS

Formation of Single-Walled Aluminosilicate Nanotubes from Molecular Precursors and Curved Nanoscale Intermediates

G. Ipek Yucelen,[†] Rudra Prosad Choudhury,[†,§] Anastasia Vyalikh,[§] Ulrich Scheler,[§] Haskell W. Beckham,[†] and Sankar Nair*[,‡]

[†]School of Materials Science and Engineering and [‡]School of Chemical & Biomolecular Engineering, Georgia Institute of Technology, Atlanta, Georgia 30332, United States

[§]Leibniz-Institut für Polymerforschung Dresden e.V., D-01069 Dresden, Germany

Supporting Information

ABSTRACT: We report the identification and elucidation of the mechanistic role of molecular precursors and nanoscale (1−3 nm) intermediates with intrinsic curvature in the formation of single-walled aluminosilicate nanotubes. We characterize the structural and compositional evolution of molecular and nanoscale species over a length scale of 0.1−100 nm by electrospray ionization mass spectrometry, nuclear magnetic resonance spectroscopy (^{27}Al liquid-state, ^{27}Al and ^{29}Si solid-state MAS), and dynamic light scattering. Together with structural optimization of key experimentally identified species by solvated density functional theory calculations, this study reveals the existence of intermediates with bonding environments, as well as intrinsic curvature, similar to the structure of the final nanotube product. We show that "proto-nanotube-like" intermediates with inherent curvature form in aqueous synthesis solutions immediately after initial hydrolysis of reactants, disappear from the solution upon heating to 95 °C due to condensation accompanied by an abrupt pH decrease, and finally form ordered single-walled aluminosilicate nanotubes. Detailed quantitative analysis of NMR and ESI-MS spectra from the relevant aluminosilicate, aluminate, and silicate solutions reveals the presence of a variety of monomeric and polymeric aluminate and aluminosilicate species (Al_1Si_x−$Al_{13}Si_x$), such as Keggin ions $[AlO_4Al_{12}(OH)_{24}(H_2O)_{12}]^{7+}$ and polynuclear species with a six-membered Al oxide ring unit. Our study also directly reveals the complexation of aluminate and aluminosilicate species with perchlorate species that most likely inhibit the formation of larger condensates or nontubular structures. Integration of all of our results leads to the construction of the first molecular-level mechanism of single-walled metal oxide nanotube formation, incorporating the role of monomeric and polymeric aluminosilicate species as well as larger nanoparticles.

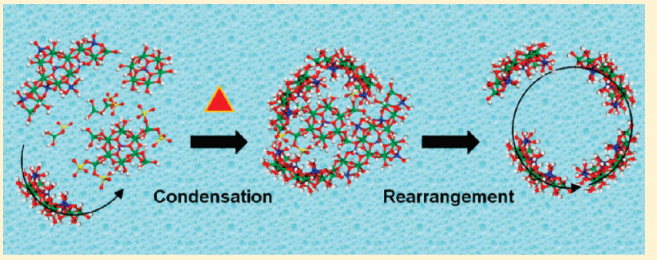

INTRODUCTION

Metal oxide nanotubes have emerged as an important class of "building block" materials for nanotechnology due to the vast range of accessible compositions and structures and their unusual electronic, optical, and mechanical properties.[1] However, only a few examples of single-walled metal oxide nanotubes are currently available, specifically aluminosilicate/germanate ($Al_2SiO_3(OH)_4$, $Al_2GeO_3(OH)_4$) and molybdenum oxide (MoO_3) nanotubes.[2,3] Their unique properties, such as well-defined wall structure and porosity, tunable dimensions, and chemically modifiable interior and exterior surfaces, make them attractive candidates for fabricating devices for molecular recognition-based applications in catalysis,[4,5] separations,[6] sensing,[2] and molecular encapsulation.[7] Furthermore, they can be synthesized by low-temperature solution-phase processes with inexpensive reactants and without the need for a catalyst.[8] A number of experimental "handles" (e.g., reactant composition, concentration, pH, temperature, energy source, and time) can therefore be applied to control the structure, dimensions, and composition of such nanotubes.[9]

The present study focuses on single-walled aluminosilicate ("AlSiOH") nanotubes, which are the synthetic analogue of the naturally occurring single-walled aluminosilicate nanotubular mineral imogolite,[10] having an outer diameter of 2.2 nm and an inner diameter of ∼1.0 nm. Their structure is well characterized based upon a number of previous studies.[10] The nanotube wall consists of a curved gibbsite $[Al(OH)_3]$ sheet with orthosilicate groups $[O_3SiOH]$ attached on the inner wall, resulting in the empirical formula $(OH)_3Al_2O_3SiOH$ (Figure 1). The structural "repeat unit" of the nanotube is composed of six aluminum oxide octahedra arranged in a hexagonal ring and coordinated to a silicate tetrahedron via three oxygen bridges (μ_3-O). There are 24 aluminum atoms in the circumference, and aluminum octahedra are linked by μ_2-OH groups at shared edges. It is believed that the attachment of the orthosilicate group causes the shortening of O−O distances from 0.32 nm in gibbsite to ∼0.27 nm,

Received: December 8, 2010
Published: March 21, 2011

 © 2011 American Chemical Society dx.doi.org/10.1021/ja111055q | J. Am. Chem. Soc. 2011, 133, 5397–5412

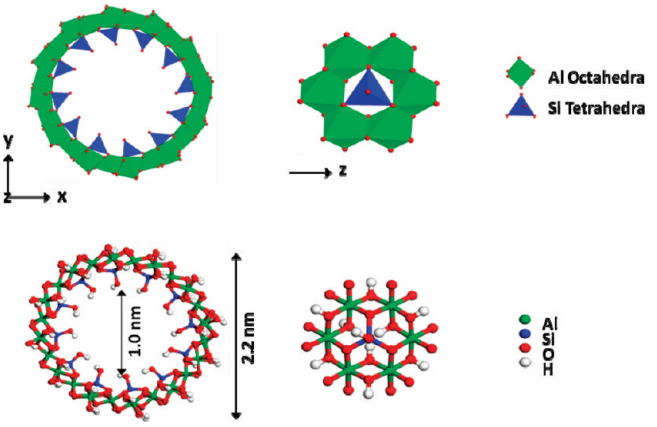

Figure 1. Ball-and-stick and polyhedron models of (left) the aluminosilicate nanotube and (right) a section of the wall showing the hexagonal aluminosilicate repeat unit. The nanotube cross-section is depicted in the *xy* plane, and the nanotube axis is in the *z* direction. The repeat unit of the nanotube has one silicate tetrahedron connected to six aluminate octahedra through three oxygen bridges.

appropriate for the edge of a SiO_4 tetrahedron.[10] Therefore, the curvature of the nanotube may be determined by the mismatch between the bond lengths on the inner and outer walls.[10] The silicate units can be completely or partially replaced with germanate tetrahedra, leading to the formation of aluminogermanate (AlGeOH) or aluminosilicogermanate (AlSiGeOH) nanotubes.[11] With increasing Ge substitution, the diameter of the tube increases and the length decreases (nanotubes as short as 20 nm can be synthesized).[2,9,11]

Apart from their emerging applications, the fundamental importance of these nanotubes lies in their use as a model system for developing a mechanistic model of self-assembly phenomena that lead to the formation of a "curved" nanostructure. The capability to engineer metal oxides into single-walled tubular materials with desired characteristics could be achieved through a detailed molecular-level understanding of their formation and growth mechanisms in the liquid phase. Such a model has not previously been available. Experimental studies so far have not been able to reveal the molecular structure of the precursors and intermediate species, which is a key step in understanding their evolution into nanotubes. However, due to the combined efforts of multiple authors, mechanistic information is available at larger length scales regarding both the initial formation of nanotubes and their subsequent growth. Formation of the aluminosilicate nanotubes has been proposed to occur from a sheet-like intermediate called "proto-imogolite", which is suggested to have an atomic arrangement similar to the final nanotube product.[12,13] However, its existence has not been proven experimentally. The existence of nanoparticle precursors with a size of ~6 nm has also been shown in previous studies[2,14] of the closely related aluminogermanate nanotube system. On the basis of inferences from dynamic light scattering (DLS) data and synthetic variations, it was proposed that these nanoparticles, which form by condensation of molecular precursors, self-assemble irreversibly into ordered nanotubular particles of ~20 nm length. Another study by small-angle X-ray scattering (SAXS) has further assigned a specific structure for this precursor nanoparticle, in particular an aluminogermanate sheet-like structure.[15] The uniqueness of this assignment is not known, especially considering previous debates on the unique interpretation of SAXS data from zeolite synthesis solutions.[16,17] However, SAXS data are valuable in determining the average particle size and polydispersity of nanoparticle precursors in solution.[18] Recent work on the synthesis of single-walled MoO_3 nanotubes[3] also suggests a cluster-based self-assembly of nanoscale precursors into nanotubes. Other studies have focused on the growth of the aluminosilicate nanotubes after their initial formation.[19] On the basis of transmission electron microscopy (TEM), electron diffraction, and DLS observations, we previously showed that large numbers of nanotubes form continuously in the synthesis solution by a self-assembly process, but that their subsequent growth is relatively much slower, thereby leading to an almost constant average length of the nanotubes as a function of synthesis time.[14] Similarly, it was shown that a 100-fold increase in the reactant concentration in the aluminogermanate nanotube synthesis had little effect on the average dimensions of the self-assembled nanotubes.[14] Nevertheless, the growth processes somewhat broaden the length distribution of the nanotubes and may occur by one or more proposed mechanisms, such as end-to-end aggregation of short nanotubes[15] and precursor addition to the nanotube ends.[19] It has also been suggested that the length distribution of the nanotubes is influenced by a slow Ostwald ripening process.[15,20]

The elucidation of the molecular precursors and intermediates in the nanotube synthesis is clearly a key "missing link" in describing the nanotube assembly. This work focuses on identifying the structure, composition, dimensions, and shapes of molecular precursors and clusters involved in the nanotube formation and tracking the evolution of these characteristics during the synthesis process. This objective is achieved by our collection and detailed analysis of electrospray ionization mass spectrometry (ESI-MS), nuclear magnetic resonance (NMR), and DLS spectra from the evolving nanotube synthesis solution and is supported with quantum chemistry calculations on several key species of interest. We conclude this paper by integrating our observations into the first molecular-scale description of the initial events in the nanotube formation process.

EXPERIMENTAL SECTION

Single-Walled Aluminosilicate Nanotube Synthesis. Tetraethoxysilane (TEOS) and aluminum *sec*-butoxide (ASB) were mixed in a glovebox filled with nitrogen and added dropwise to ~0.05 M aqueous solution of $HClO_4$ in the molar ratios Si:Al:$HClO_4$ = 1:2:1 at 25 °C. The solution was vigorously stirred and aged for 18 h at 25 °C and then diluted to 0.02 M in Al. Immediately after dilution, the temperature was increased to 95 °C and kept constant under vigorous stirring for 4 days (96 h). At the end of the reaction sequence, the nanotubes were first precipitated by dropwise addition of a 30 wt % ammonia solution. The resulting gel was centrifuged, the supernatant was discarded, and 10 N HCl was added dropwise to redisperse the nanotubes. Finally, the dispersion was dialyzed for 4 days against deionized water using a 15 kDa membrane to obtain a pure nanotube dispersion. Nanotube powder was obtained by drying the dialyzed nanotube solution at 60 °C in an oven.

Samples for liquid-state NMR and ESI experiments were directly taken from the synthesis reactor at various stages during the 18 h aging stage (at 25 °C) and the subsequent 96 h heating stage (at 95 °C). Samples were immediately used for characterization. Solid-state NMR samples were prepared by freeze-drying solutions at −50 °C for 5 days. All NMR and ESI characterizations were carried out at room temperature (25 °C).

^{27}Al Liquid-State NMR Spectroscopy. Liquid samples of 600 μL volume were placed in 5-mm glass NMR tubes and diluted with a 90% H_2O/10% D_2O mixture, which acted as a field frequency lock. Single-pulse ^{27}Al liquid-state NMR spectra were collected on a Bruker DMX 400 instrument at a frequency of 104.2 MHz. A total of 10k free induction decays were recorded with a repetition time of 0.1 s. The pulse width and acquisition time were 7.5 μs and 0.25 s, respectively. The spectra were carefully corrected for background signals due to aluminum-containing ceramics in the probe by subtracting a spectrum obtained from a "blank" H_2O/10% D_2O solution. Chemical shifts are referenced to a 0.1 M $AlCl_3$ solution.

^{27}Al Solid-State Magic Angle Spinning NMR Spectroscopy. For NMR measurements, the samples were packed into 4-mm-o.d. tightly capped zirconium rotors. ^{27}Al solid-state NMR measurements were performed on a 11.7 T Bruker Avance 500 spectrometer operating at resonance frequencies of 130.34 MHz for ^{27}Al and 500.13 MHz for ^{1}H. ^{27}Al chemical shifts were referenced externally to the $AlCl_3$ aqueous solution at 0 ppm. ^{27}Al MAS NMR spectra were acquired at a spinning frequency of 14 kHz employing a BL4 HXY 4 mm MAS probehead with ^{1}H decoupling. A single pulse of 1 μs duration was applied to ensure quantitative excitation. A recycle delay of 1 s and 512 repetitions were used. Quantitative analyses of the ^{27}Al MAS NMR spectra were done by using DMFIT software.[21]

^{29}Si Solid-State CP-MAS NMR Spectroscopy. ^{29}Si solid-state CP-MAS NMR spectra were recorded on a Bruker DSX 300 spectrometer with a 7-mm rotor at a spinning rate of 6 kHz. ^{1}H and ^{29}Si frequencies were 300.2 and 59.6 MHz, respectively. Chemical shifts were referenced to 3-(trimethylsilyl)-1-propanesulfonic acid sodium salt. The standard cross-polarization ^{1}H−^{29}Si pulse sequence was performed with 5 s recycle delay between pulses and 3 ms contact time. The 90° pulse length was 5 μs. The data represent 2048 transients processed with a 5 Hz line broadening.

Electrospray Ionization Mass Spectrometry. A Quattro LC (quadrupole−hexapole−quadrupole) mass spectrometer with an orthogonal Z-spray electrospray interface was used. The temperature of the surface block was 100 °C, and the temperature of the desolvation gas was 150 °C. Samples were injected into the ESI-MS immediately after they were taken from the nanotube synthesis reactor. The samples were not diluted. Capillary voltages of 3.3 kV for negative scan mode and 3.5 kV for positive scan mode were used. The optimum cone voltage was determined to be 50 V via control experiments on aluminate and silicate samples. Information on species present in these solutions was difficult to extract from spectra obtained at lower cone voltages, and higher cone voltages were not used to avoid the possibility of fragmentation of the species. Nitrogen was used as the drying gas and nebulizing gas at flow rates of 500 and 100 L/h, respectively.

Dynamic Light Scattering. DLS measurements were made at 25 °C with a DynaPro instrument at a wavelength of 589 nm. Prior to measurements, solutions were filtered through a 0.2-μm filter to remove any dust particles. The scattering angle was 90°. The number of scans was 20, with a 10 s acquisition time per scan.

Molecular Modeling. Density functional theory (DFT) calculations were performed using the DMol^3 package in the Materials Studio molecular modeling software (Accelrys). Energies are calculated using the generalized gradient approximation (GGA) and the BLYP functional to model exchange and electron correlation effects. Thermal smearing is applied to accelerate convergence. Many of the species identified by ESI-MS already possess an explicit first hydration shell of water and hydroxyl groups. Longer-range solvent effects are also included using the conductor-like screening model (COSMO).[22] Since some of the species contain Cl atoms, spin-unrestricted ground-state energy calculations were performed in all cases for consistency. A double-numerical plus d functions (DND) effective core potential basis set was employed in all calculations. The effect of using a highly accurate double-numerical plus polarization functions (DNP) effective core potential basis set was then studied using a few test species. In all cases, there was very little change in the optimized geometries from the DND basis set calculations. Vibrational frequency calculations were then used to verify convergence to energy minima. To accelerate the tedious vibrational frequency calculations, this step was performed using a double-numerical (DN) basis set.

RESULTS AND DISCUSSION

Characterization of Nanotube Synthesis Solution by Liquid-State NMR. We used liquid-state ^{27}Al and solid-state ^{27}Al and ^{29}Si NMR spectroscopy to examine aluminosilicate nanotube formation from the precursors ASB and TEOS in mildly acidic aqueous solutions, as a function of aging time (up to 18 h at 25 °C) and subsequent heating at elevated temperature (up to 96 h at 95 °C). Some low-symmetry species may not be detected by liquid-state ^{27}Al NMR due to the quadrupolar interaction of ^{27}Al nuclei.[23] To examine the issue of any Al environments undetected by liquid-state NMR, we therefore also performed ^{27}Al solid-state MAS NMR on freeze-dried samples taken at various stages of the nanotube synthesis. Attempts to perform liquid-state ^{29}Si NMR studies on nanotube solutions were unsuccessful due to the low isotopic abundance and low sensitivity of ^{29}Si nuclei. Signal enhancement methods that depend on polarization transfer from ^{1}H (e.g., INEPT)[24] were also unsuccessful. Hence, all ^{29}Si NMR studies were performed in the solid state.

The ^{27}Al liquid-state NMR spectra show two sharp and distinct resonances corresponding to the six-coordinated octahedral monomer $[Al(H_2O)_6]^{3+}$ ($\delta_{Al(VI)} \approx 0$ ppm) and a four-coordinated aluminum environment ($\delta_{Al(IV)} = 63.3$ ppm) which begins to disappear upon heating, as well as a broader peak near 6 ppm that falls in the six-coordinated chemical shift region (Figure 2). The peak at 63.3 ppm is due to a tetrahedral Al unit at the center of a highly symmetric (Al_{13}) $[AlO_4Al_{12}(OH)_{24}(H_2O)_{12}]^{7+}$ species.[25] The nanoscale Keggin-like species is well-known to be present in acidic aluminate solutions[26] and contains a central tetrahedral Al coordinated with 12 surrounding Al octahedra via four oxygen atoms at each vertex of the tetrahedron (Figure 3). The ^{27}Al NMR line from the surrounding octahedral aluminums is nearly invisible due to quadrupolar broadening and was only revealed at 12 ppm[27,28] after deconvoluting the spectra obtained during the aging stage (Supporting Information Figure S1a,b). The inset in Figure 2 shows the single ^{27}Al NMR resonance ($\delta_{Al(VI)} \approx 6$ ppm) from a pure nanotube suspension after dialysis. Therefore, the broad peak centered around 6 ppm that was observed throughout the synthesis is assigned to six-coordinated Al species with a bonding environment very similar to that found in the nanotube structure (i.e., hexagonal aluminosilicate repeat units as shown in Figure 1). As evident from Figure 2, this environment, corresponding to the "nanotube-like" structure, exists throughout the synthesis (aging and heating stages) together with the monomeric Al species.

The evolution of local environment around the Al atoms is examined by tracking the chemical shifts, line widths, and integrated areas of the measured resonances (Figure 4 and Supporting Information Figures S2 and S3). The NMR spectra collected at various stages of the synthesis were fit with a series of Lorentzian peaks to obtain the position, full width at half-maximum (fwhm), and area of each peak (Supporting Information Figure S1). In particular, tracking the 6 ppm resonance provides information regarding the evolution of Al

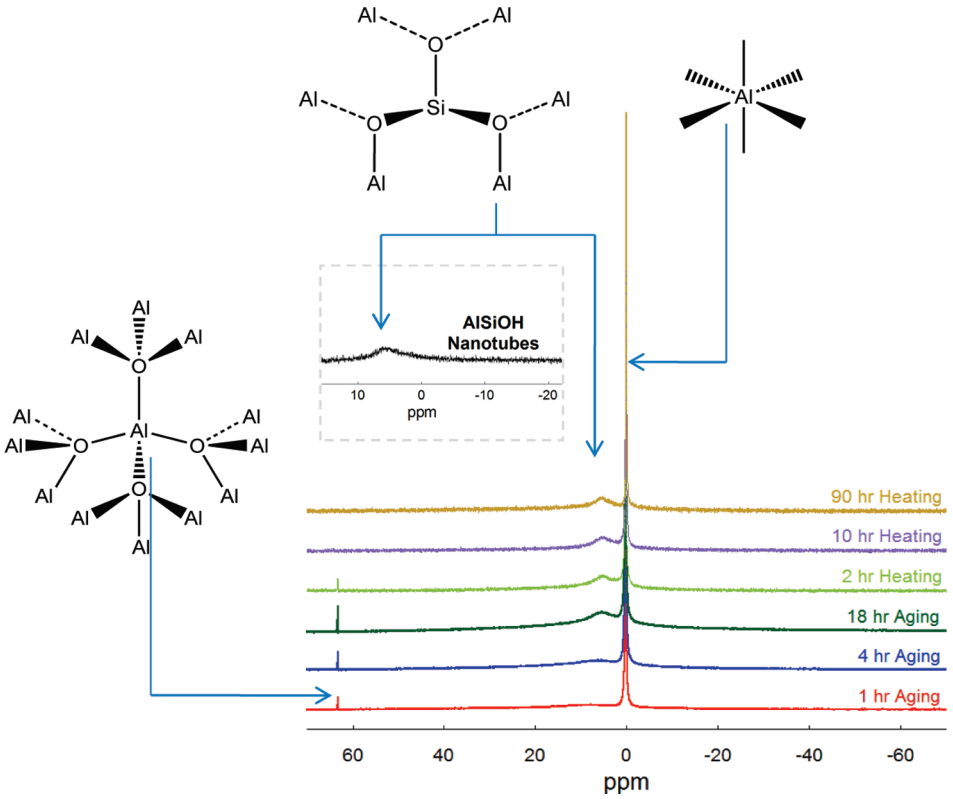

Figure 2. ^{27}Al liquid-state NMR spectra of nanotube solutions at various stages of aging (25 °C) and heating (95 °C). The inset shows ^{27}Al NMR resonance of dialyzed aluminosilicate nanotube solution ($\delta_{Al(VI)} \approx 6$ ppm). Spectra were collected at 25 °C. The species assigned to each NMR signal are shown by 2D ChemDraw representations. The peak at 63.3 ppm is observed during aging of nanotube synthesis solutions at 25 °C and is assigned to the tetrahedral aluminum at the center of a Keggin polycation. This peak disappears within 7 h of heating. The peak near 6 ppm is assigned to octahedral aluminum in a "nanotube-like" coordination environment. The sharp peak near 0 ppm represents octahedral monomer aluminate units.

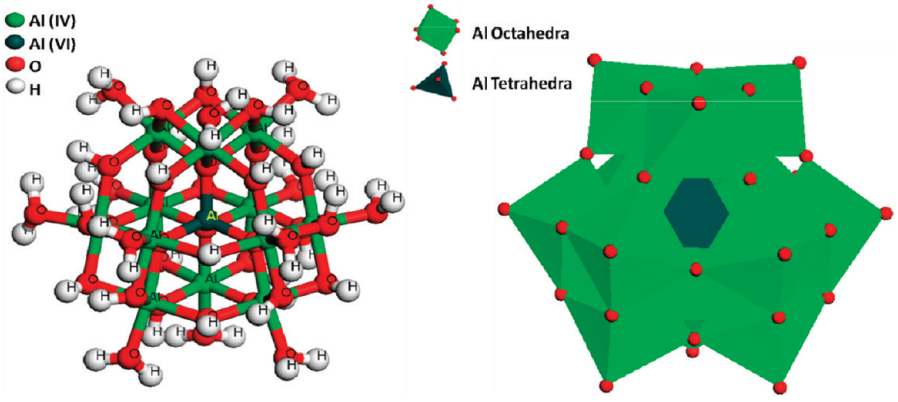

Figure 3. Ball-and-stick model (left) and polyhedron model (right) of the Keggin cation $[AlO_4Al_{12}(OH)_{24}(H_2O)_{12}]^{7+}$. The Keggin cation consists of a tetrahedral aluminate $[AlO_4]^{5-}$ center surrounded by four octahedral aluminate $[Al_3(OH)_6(H_2O)_3]^{3+}$ trimer units.[28,29]

configurations that resemble the nanotube wall structure. Moreover, the line widths of ^{27}Al NMR resonances are strongly dependent on the symmetry (i.e., electric field gradient) of the species.[23]

The peak chemical shift of the broad octahedral ^{27}Al NMR signal decreases from 8.5 ppm to 5.5 ppm and its fwhm decreases from 13 ppm to 8 ppm (Figure 4a,b) during the aging stage, likely due to local atomic ordering around Al in the nanotube-like configuration. After 7 h aging at 25 °C, these values become stable, indicating that a stable species with an ordered nanotube-like configuration of the octahedral Al has been formed in the aging process. Moreover, the integrated intensities of this peak, as well as that of the Al_{13} species (63.3 ppm), increase as a function of aging time but nearly reach a plateau after 18 h of aging (Figure 4c,d). Concurrently, the integrated area of the monomer peak at ~0 ppm decreases during the aging step (Figure 4e). Thus, the nanotube-like species and Keggin ions increase at the expense of the monomer species as equilibrium is established. Upon heating of the aged solution to 95 °C, the signal at 63.3 ppm disappears within 7 h (Figure 2 and Supporting Information

dx.doi.org/10.1021/ja111055q | J. Am. Chem. Soc. 2011, 133, 5397–5412

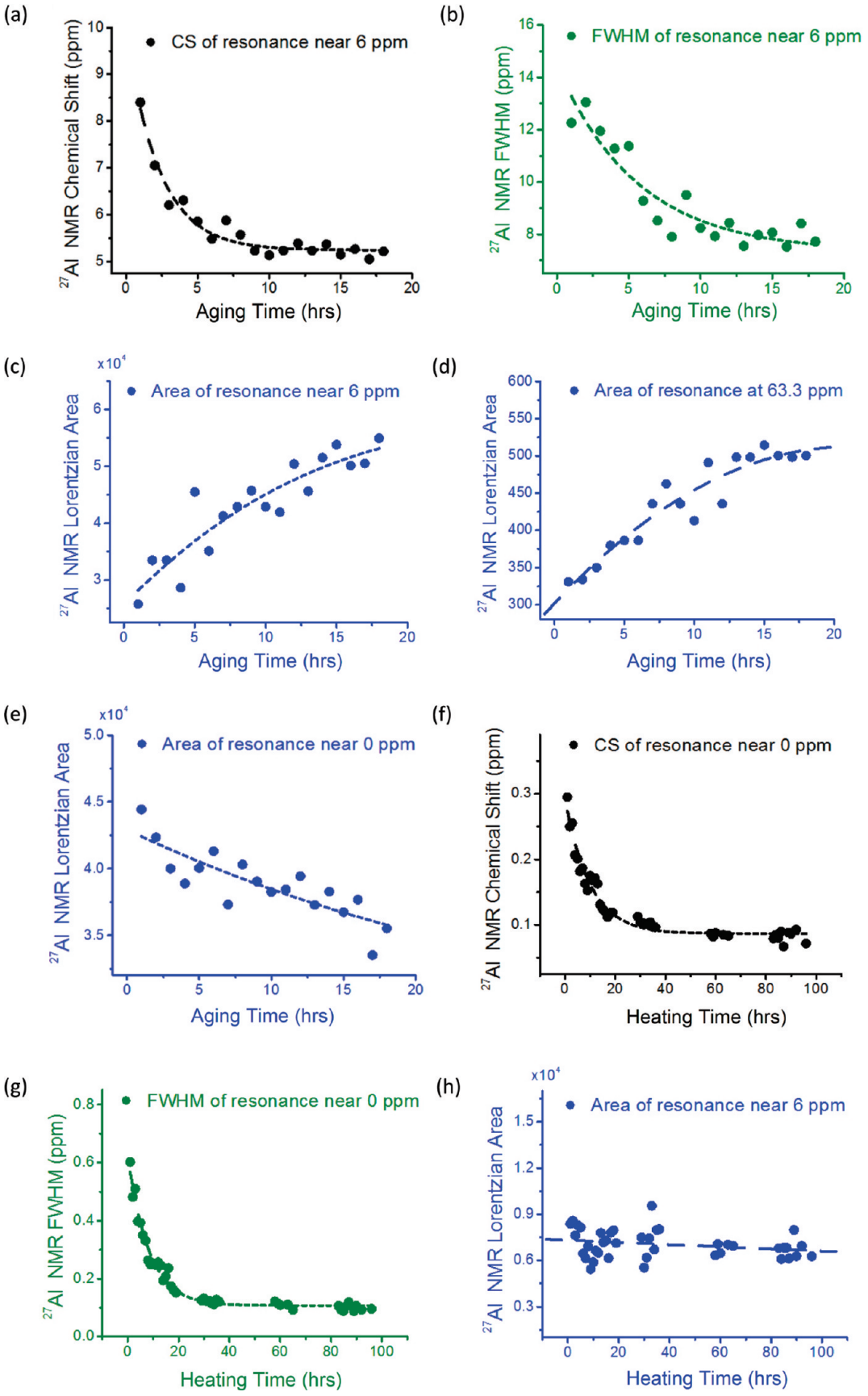

Figure 4. Chemical shift (CS), fwhm, and integrated areas (arbitrary units) of resonances in ^{27}Al liquid-state NMR spectra of evolving nanotube synthesis solution. The lines are least-squares fits to guide the eye. See text for detailed discussion.

dx.doi.org/10.1021/ja111055q |*J. Am. Chem. Soc.* 2011, 133, 5397–5412

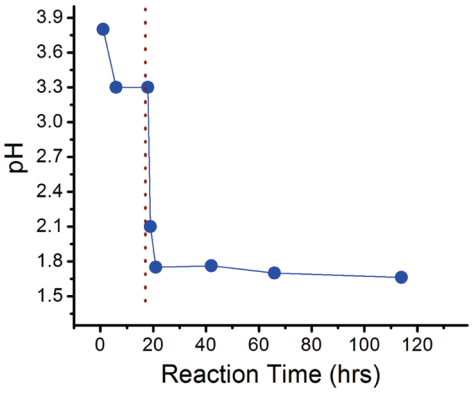

Figure 5. pH change of the nanotube synthesis solution as a function of reaction time. The dotted line separates the aging (left) (25 °C) and heating (right) (95 °C) stages.

Figure S3b). A previous study of pure aluminate solutions suggests that the disappearance of the 63.3 ppm signal above 90 °C is due to clustering and rearrangement of the Keggin clusters to hexameric rings, which are appropriate precursors for gibbsite (layered $Al(OH)_3$) and boehmite (layered AlOOH) formation.[30] Such rearrangements should result in the broadening of the 63.3 ppm resonance[25] due to a breaking of the tetrahedral symmetry but is not observed in our study. The chemical shift of the monomer decreases from 0.3 ppm to 0.1 ppm within 24 h of heating, and its fwhm also decays and levels off in a similar manner (Figure 4f,g). These small changes can be explained by a shift in the equilibrium between aluminate monomers:[25,30] $[Al(H_2O)_6]^{3+} \leftrightarrow [Al(H_2O)_5(OH)]^{2+} + [H]^+$. As explained later in this report, this equilibrium shift is clearly seen as a change of pH of the evolving nanotube synthesis solution.

No significant changes are observed in the chemical shift, integrated area, and line width of the broad octahedral peak near 6 ppm during the heating step (Figure 4h and Supporting Information Figure S3a,d). This result strongly indicates that no significant new Al coordination environments are formed during the heating step and that the same Al-containing species formed in the aging step are participating in nanotube formation, albeit with some minor structural changes. The precursors necessary for nanotube formation should therefore already be in the solution prior to heating and would be used in the formation of nanotubes during the heating stage.

Deconvolution of the heating stage spectra (Supporting Information Figure S1c,d) also revealed a new broad peak at 3−5 ppm in the octahedral coordination region, whereas the 12 ppm peak detected during aging, belonging to octahedral units of the Keggin ion, has disappeared after 1 h of heating. These simultaneous events suggest either a change in equilibrium between two species or breakdown of Al_{13} into species represented by the 3−5 ppm peak upon heating. Moreover, the changes in chemical shift of the 3−5 ppm peak are strongly correlated to that of the monomer peak (Figure 4f,g and Supporting Information Figure S3c). This may also indicate an equilibrium between these two species during the heating stage. The ^{27}Al NMR peak near 3−5 ppm might be attributed to dimeric[23] or trimeric[31] aluminate species. According to Akitt,[32] there is an equilibrium between three species in hydrolyzed acidic aluminate solutions: $[Al(H_2O)_6]^{3+} \leftrightarrow [Al_2(OH)_2(H_2O)_8]^{4+} \leftrightarrow [AlO_4Al_{12}(OH)_{24}(H_2O)_{12}]^{7+}$. A similar equilibrium between Al_1Si_x, Al_2Si_x, and Al_3Si_x species and a Keggin-like $Al_{13}Si_x$ metastable complex[32,33] can explain the above observed behavior of the 0 ppm and 3−5 ppm peaks, together with the disappearance of the Keggin signal at 12 ppm. Another possibility is that the 12 ppm peak may have disappeared due to the increased quadrupolar broadening caused by condensation of Keggin molecules, although clear evidence for this speculation was not found in our study. In summary, our liquid-state ^{27}Al NMR experiments and analysis provide substantial information on the species formed and on their evolution. For the first time, Keggin species were identified clearly in the nanotube synthesis solution.

Figure 5 shows the change in pH as a function of aging and heating time. After initial mixing of reactants at 25 °C, the pH drops from ∼3.7 to 3.3 within 7 h. The pH further drops precipitously to ∼1.7 immediately after the onset of heating to 95 °C and thereafter stays nearly constant throughout the reaction. The large drop in pH denotes a precursor condensation[13,30,34] leading to a release of protons. We therefore conclude that the combined observations in the aging step—decrease in line width, increase in integrated area, and decrease in chemical shift of the peak near 6 ppm; decrease in monomer peak intensity; increase in the Keggin signal; and slight decrease in pH—clearly indicate an equilibrium established between the monomers, Keggin ions, and species with nanotube-like coordination environment at 25 °C. Upon increasing the temperature to 95 °C, a condensation and rearrangement process takes place. The equilibrium between species shifts, and the Keggin ion decomposes. Trimeric and dimeric species are likely to be formed in addition to the monomers and the species with nanotube-like coordination. These events are also supported by our ESI-MS study, discussed later in this report.

Characterization of Nanotube Synthesis Solution by Solid-State NMR. The ^{27}Al MAS NMR spectrum of the pure nanotube powder (Figure 6a) shows an intense peak at 7 ppm, corresponding to octahedral aluminum. Another small and broad peak at 60−63 ppm is also observed, corresponding to tetrahedral aluminum. Since the presence of the tetrahedral sites is not expected in the nanotube wall,[2,14] they are likely present on the ends of the nanotube. The resonance corresponding to the octahedral sites does not show sharp features characteristic of the quadrupolar line shape in powder solids.[35] The orientation, bundling, or bending of the nanotubes may result in a distribution of spectral parameters and therefore may cause additional broadening that smears out the feature of the quadrupolar line shape.

The parameters of the quadrupolar interaction and isotropic chemical shifts (δ_{ISO}) for the different ^{27}Al sites—one tetrahedral and two octahedral aluminums—have been used to model and quantify the experimental spectrum of pure nanotubes (Figure 6a). One of the octahedral sites is considered with a Gaussian isotropic model (GIM) wherein the statistical distribution of the quadrupolar interaction (and thus broadening) is implemented. The MAS NMR spectra of the quadrupolar nuclei with a distribution of quadrupole parameters are well characterized by the GIM model.[36−39] This model includes a quadrupolar coupling constant (C_{Qmax}), which is the maximum likelihood of the quadrupolar coupling constants (C_Q) in the GIM distribution corresponding to $\sim 2\sigma$ in the Czjzek distribution equation.[21,40] After optimization of the model fit, two octahedral peaks at 9 ppm and 4 ppm are found. The octahedral peak at 9 ppm, with $C_Q = 2.9$ MHz, accounts for 75% of the total intensity.

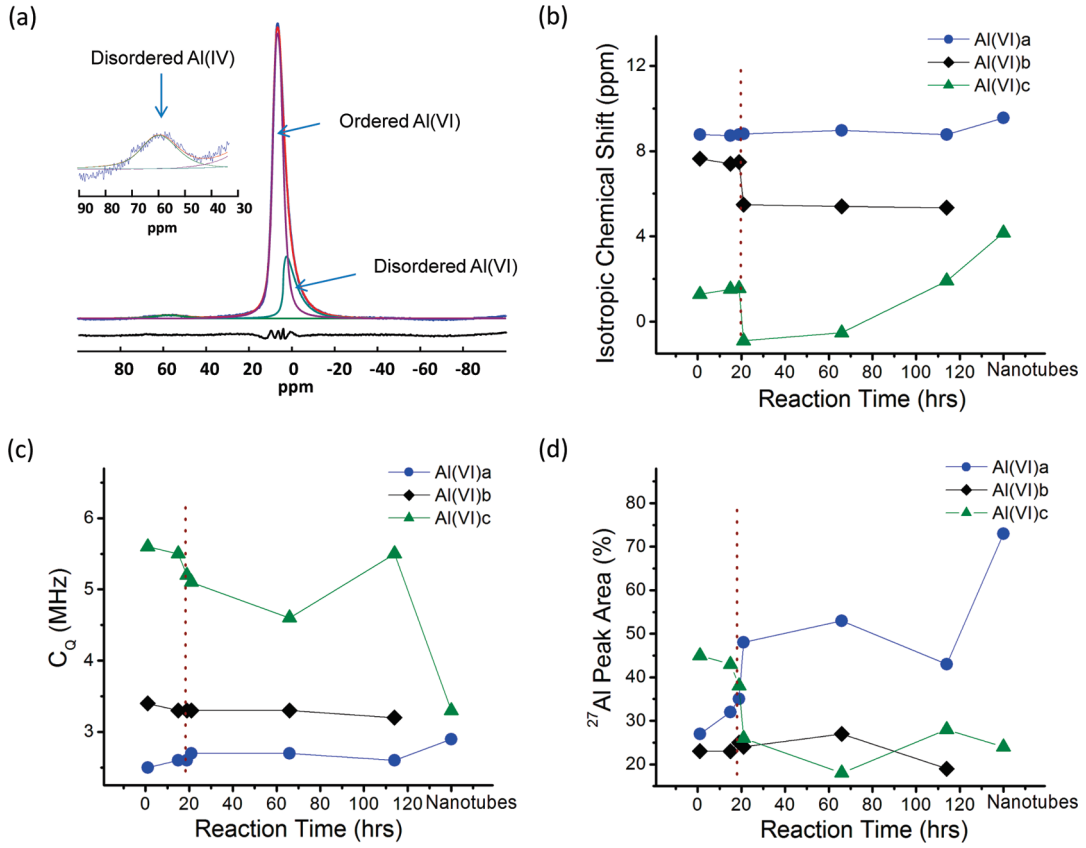

Figure 6. (a) ^{27}Al MAS spectra of dialyzed and subsequently oven-dried (60 °C) nanotube powder and its decomposition with three components (peaks near 60−63 ppm, 9 ppm, and 4 ppm, respectively). The difference between the generated fit and the experimental spectrum is shown at the bottom. Inset is a magnification of the region 30−90 ppm of the main NMR spectra. As discussed in the text, this peak represents tetrahedral conformations of aluminum atom. (b) Isotropic chemical shift and (c) quadrupolar coupling constant of the octahedral ^{27}Al species observed after deconvolution of the MAS spectra of the evolving nanotube synthesis solution. (d) Evolution of peak area of the Al(VI) species observed after deconvolution of the MAS spectra of the sample taken versus synthesis time. The dotted line separates the aging (left) and heating (right) stages. The data point after the end of the reaction represents the dialyzed nanotubes.

This peak, labeled as Al(VI)a, has a negligible distribution of quadrupole parameters. It represents the major part of the nanotube structure, with the ^{27}Al sites arranged in a perfectly ordered manner on the nanotube wall. The isotropic chemical shift of the other octahedral peak, wherein the distribution of quadrupole parameters is found to be significant, occurs at 4 ppm and with C_{Qmax} = 3.4 MHz. This resonance is labeled as Al(VI)c and is also a part of the nanotube structure. It may present a distribution of the spectral parameters due to different orientations, bundling, or bending of the nanotubes. Along with the tetrahedral site, it represents the "disordered" Al sites of the nanotube material, on which liquid-state NMR was not able to provide information.

The experimental solid-state ^{27}Al MAS spectra of the freeze-dried samples, taken at various stages of the nanotube synthesis, were then modeled and analyzed with three octahedral sites along with a tetraaluminum species (Supporting Information Figure S4). The evolution of the three octahedral sites during the reaction is examined by tracking the isotropic chemical shifts and the quadrupolar coupling constant of the respective sites and given in Figure 6b,c. The integrated areas of these three signals are given in Figure 6d. The site with δ_{ISO} = 9 ppm and C_Q = 2.7 MHz corresponds to the major signal component of the dialyzed nanotube, as discussed previously. Hence, this site is labeled as Al(VI)a. Considering the high stability of its chemical shift and C_Q during the reaction (Figure 6b,c), it can be concluded that species with nanotube-like configuration are present in the reaction mixture from the beginning of the aging step and evolve into ordered nanotubes with time (Figure 6d).

On the other hand, the signal from the Al(VI)c possessing a statistical distribution of the quadrupolar interaction decreases with increasing reaction time. The initial δ_{ISO} and the C_{Qmax} of Al(VI)c are 1 ppm and 5.5 MHz, respectively (Figure 6b,c). Considering the high value of C_{Qmax} and the nature of its distribution, it can be concluded that this site represents the disordered component of the reaction mixture, which gradually converts to the nanotube-like structure. As a result, its signal intensity (Figure 6d) decreases with increasing reaction time. Another octahedral site, wherein the δ_{ISO} is initially 7 ppm and $C_Q \approx 3.4$ MHz, does not show any significant changes throughout the reaction time. This site is not present in the dialyzed nanotubes and is labeled as Al(VI)b. This site may represent different oligomeric aluminum species coordinated with perchlorate or silicate ions. These species are also observed in our ESI-MS studies (*vide infra*). The intensity of the tetra-coordinated aluminum signals nearly disappear a few hours into the heating. This behavior was also observed in a previous ^{27}Al MAS NMR study and was explained as a rehydration of tetrahedral

dx.doi.org/10.1021/ja111055q |*J. Am. Chem. Soc.* 2011, 133, 5397–5412

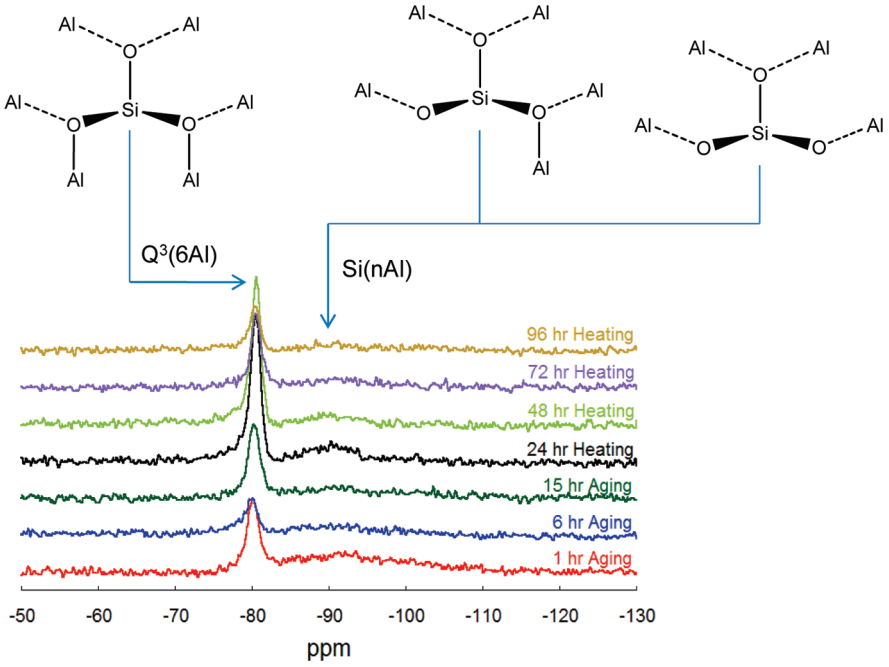

Figure 7. ^{29}Si CP-MAS NMR spectra of freeze-dried nanotube solutions as a function of synthesis time. Measurements are done at 25 °C. The peak at −80 ppm is due to the characteristic Q^3(6Al) configuration of Si in the aluminosilicate nanotube. The broad peak centered near −90 ppm is assigned to silicon tetrahedra surrounded by n = 1−5 aluminum atoms. Tentative representations of Si(5Al) and Si(4Al) are shown above the NMR spectra.

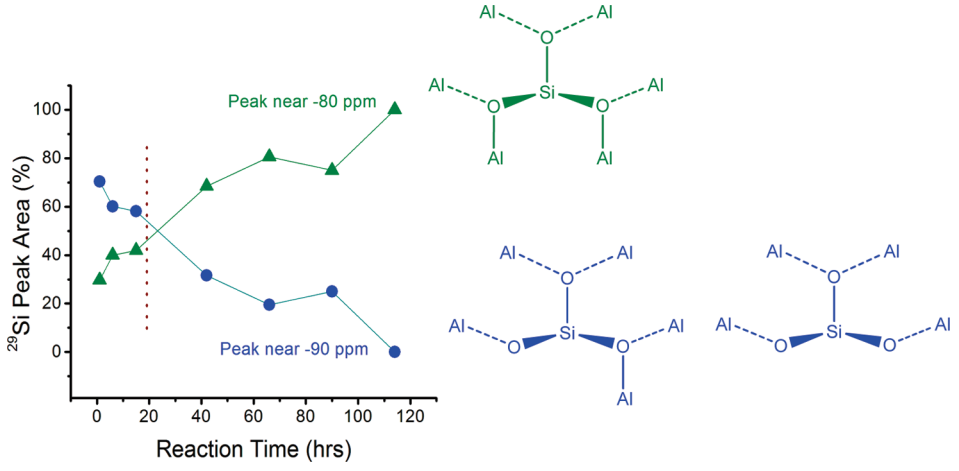

Figure 8. Integrated areas (relative to the total area) of the two resonances (peaks centered at −80 and −90 ppm) in the ^{29}Si CP-MAS NMR spectra versus reaction time (18 h aging at 25 °C followed by 96 h heating at 95 °C). The dotted line separates the aging (left side) and heating (right side) stages. Spectra were collected at 25 °C.

aluminum to octahedral aluminum prior to proto-nanotube (proto-imogolite) formation.[13]

The ^{29}Si CP-MAS NMR spectra of freeze-dried aluminosilicate nanotube solutions at various stages of the synthesis are shown in Figure 7. In aluminosilicate materials, ^{29}Si chemical shifts and line widths are affected by coordination with aluminum and the aluminum distribution in the lattice [Si(nAl), with n being the number of next-nearest-neighbor Al atoms].[41] The ^{29}Si CP-MAS NMR spectra exhibit a broad resonance centered near −90 ppm (limits range from −75 to 110 ppm) and a sharp peak at −80 ppm. Tetrahedral silicon groups attached to three Al atoms in a Q^3(6Al) coordination are known to give rise to a sharp resonance near −80 ppm.[42] These results indicate the existence of Q^3(6Al) coordination throughout the synthesis, as also confirmed by our ^{27}Al NMR studies due to the peak near 6−7 ppm. The broad line width of the other resonance (centered at −90 ppm) is assigned to variation in the local silicon coordination arising from the individual Si(nAl) [n = 1−5] coordination environments and their characteristic ^{29}Si NMR chemical shifts separated approximately by 5 ppm and known to resonate within the range of −75 to −110 ppm.[43−45]

As shown in Figure 8, the integrated area % of the −90 ppm peak (relative to the total integrated area) gradually decreases, whereas that of the −80 ppm peak increases. This indicates the transformation of disordered Si environments to ordered Q^3(6Al) nanotube-like configurations. On the other

dx.doi.org/10.1021/ja111055q |J. Am. Chem. Soc. 2011, 133, 5397–5412

Table 1. Aluminate Complexes Identified from Positive and Negative Charge Scan Modes of ESI-MS (m/z 20−900) in Mildly Acidic Solutions (pH ~3.4) after 1 h of Hydrolysis of ASB at 25 °C

chemical formula of Al species detected at 25 °C	peak series (m/z)
ESI (+)	
$[Al(OH)_2(H_2O)_n]^+$	$61 + 18n$ ($n = 0-2$)
$[Al(OH)(H_2O)_n(ClO_4)]^+$	$143 + 18n$ ($n = 0-3$)
$[Al(H_2O)_n(ClO_4)_2]^+$	$225 + 18n$ ($n = 0-3$)
$[Al_2(OH)_4(H_2O)_n(ClO_4)]^+$	$221 + 18n$ ($n = 0-5$)
$[Al_2(OH)_3(H_2O)_n(ClO_4)_2]^+$	$303 + 18n$ ($n = 0-5$)
$[Al_2(OH)_2(H_2O)_n(Cl^{35}O_4)_2(Cl^{37}O_4)]^+$	$387 + 18n$ ($n = 0-4$)
$[Al_5(OH)_9(H_2O)_{n+5}(ClO_4)_4]^{2+}$	$387 + 9n$ ($n = 0-6$)
$[Al_7(OH)_{17}(H_2O)_{7+n}(Cl^{35}O_4)_2]^{2+}$	$401 + 9n$ ($n = 0-4$)
$[Al_{10}(OH)_{22}(H_2O)_n(Cl^{35}O_4)_5(Cl^{37}O_4)]^+$	$420 + 18n$ ($n = 0-2$)
$[Al_6(OH)_{17}(H_2O)_n]^+$	$451 + 18n$ ($n = 0-2$)
$[Al_7(OH)_{15}(H_2O)_{n+5}(ClO_4)_4]^+$	$465 + 18n$ ($n = 0-3$)
$[Al_8(OH)_{17}(H_2O)_n(Cl^{35}O_4)_4(Cl^{37}O_4)]^{2+}$	$501 + 9n$ ($n = 0-4$)
$[Al_8(OH)_{17}(H_2O)_{n+2}(Cl^{35}O_4)_2(Cl^{37}O_4)]^{2+}$	$515 + 9n$ ($n = 0-4$)
$[Al_9(OH)_{22}(H_2O)_{n+8}(Cl^{35}O_4)_3]^{2+}$	$529 + 9n$ ($n = 0-2$)
$[Al_9(OH)_{20}(H_2O)_{n+9}(Cl^{35}O_4)_4(Cl^{37}O_4)]^{2+}$	$621 + 9n$ ($n = 0-4$)
$[Al_{13}O_4(OH)_{24}(H_2O)_{n+2}(Cl^{35}O_4)_4(Cl^{37}O_4)]^{2+}$	$678 + 9n$ ($n = 0-5$)
$[Al_8(OH)_{22}(H_2O)_{n+2}(Cl^{35}O_4)]^+$	$707 + 18n$ ($n = 0-2$)
$[Al_{12}O_4(OH)_{20}(H_2O)_{n+4}(Cl^{35}O_4)_5(Cl^{37}O_4)]^{2+}$	$698 + 9n$ ($n = 0-5$)
ESI (−)	
$[Cl(O)_{n+3}]^-$	$83 + 16n$ ($n = 0-1$)
$[Al_2O_3(OH)]^-$	m/z 119
$[Al(ClO_4)_4]^-$	m/z 425
$[Al(OH)(ClO_4)_3]^-$	m/z 341

hand, from our ^{27}Al liquid-state NMR results we know that the fraction of species with nanotube-like configuration (peak near 6 ppm) does not increase to a significant extent as a function of reaction time. Therefore, we believe that the increase in relative intensity of the −80 ppm peak is a result of ordering (e.g., lattice formation) of aluminum atoms that are already in a nanotube-like coordination with the Si species [Si(nAl) → Si(6Al)] and not due to significant new formation of Q^3(6Al) configurations. The ^{29}Si chemical shift near −80 ppm of the evolving solutions does not change, showing that the Si(6Al) chemical environment of silicon remains stable throughout the synthesis. The chemical shift of the peak centered at −90 ppm also remains constant, but it gradually diminishes during the reaction.

Aluminum and Silicon Speciation in Mildly Acidic Solutions. Before examining the nanotube synthesis solution, we first conducted ESI-MS experiments on ASB (0.1 M, pH 3.5, at 25 °C) and TEOS (0.05 M, pH 3.2, at 25 °C) solutions hydrolyzed in perchloric acid to understand aluminum and silicon speciation in mildly acidic aqueous solutions. The ESI-MS technique has the ability to "gently" vaporize and transfer ions directly from solutions to the gas phase in the mass spectrometry column, thereby allowing rapid and highly sensitive characterization of molecular species and larger complexes.[46,47] The ESI-MS spectra of ASB and TEOS solutions after 1 h of hydrolysis at 25 °C are shown in Supporting Information Figures S5 and S6. The structural identification of hydrolysis products is carried out on the basis of the detected mass-to-charge ratio (m/z), isotopic ratios, and "water (H_2O) series", which are signals with incremental differences of m = 18 units (corresponding to the same species with different numbers of attached water molecules in the vaporized state). Therefore, the m/z separation between the signals will be 9 units for doubly charged species and 6 units for triply charged species.[48−50] Peaks that do not belong to a water series cannot be identified immediately, as their charge cannot be inferred *a priori*. Care is required in order to extract the relevant information from the large mass of ESI-MS data.[51] We adopted a detailed quantitative approach. A computer code was written in order to scan through all possible molecular formulas that match every detected peak (m/z ratio) above noise level. The code considers all elemental combinations (including all chemically significant isotopes) of Al, Si, H, O, C, and Cl, as well as every ligand (−OH, −Cl, $-OCl^{35}O_3$, $-OCl^{37}O_3$, $-OC_2H_5$, $-OC_4H_9$). This produced a list of arithmetically possible molecular formulas, of which the vast majority are easily eliminated as being chemically impossible. The final lists of aluminate and silicate species in Tables 1 and 2 were assigned to the experimental m/z ratios on the basis of their full agreement with the interpreted charge, isotope separation, and structural consistency throughout the spectra. Moreover, the last m/z ratio of a "water series" should not exceed the number of available coordination sites for water in the identified structure. On the other hand, the chlorine isotopic distribution patterns in the m/z 400−900 region indicate several complexes with overlapping m/z values. In this region, it is much more difficult to identify the large number of isotope peaks and to correlate the isotope peak ratios to the amount of chlorine in the structure. For example, the isotopic peak intensity ratio should be 9:6:1 for species containing two $OClO_3^-$ ions, but because of overlapping of signals from different species, this ratio is not easily identified.[52] Finally, solvated DFT calculations were used to optimize the geometry of selected hydrolysis products.

Several aluminate species of varying sizes, containing 1−13 aluminum atoms (Al_1−Al_{13} species), were identified (Table 1). Small molecules were observed in various forms, including monomeric complexes $[Al(OH)_2(H_2O)_n]^+$ (n = 0−2), $[Al(OH)(H_2O)_n(ClO_4)]^+$ (n = 0−3), $[Al(H_2O)_n(ClO_4)_2]^+$ (n = 0−3), $[Al(OH)(ClO_4)_3]^-$, $[Al(ClO_4)_4]^-$, and $[Al(OH)_3(H_2O)_n(ClO_4)_3]^-$; dimers $[Al_2(OH)_4(ClO_4)(H_2O)_n]^+$ (n = 0−5), $[Al_2(OH)_3(H_2O)_n(ClO_4)_2]^+$ (n = 0−5), and $[Al_2(OH)_2(H_2O)_n(Cl^{35}O_4)_2(Cl^{37}O_4)]^+$ (n = 0−4), $[Al_2O_3(OH)]^-$; and trimers $[Al_3O_3(OH)(H_2O)_n(ClO_4)_3]^-$ (n = 0−4). As seen in the geometry-optimized structures (Figure 9) of singly or multiply charged $[Al_6]^+$ and $[Al_8]^{2+}$ polymeric aluminate complexes, there are complete or incomplete aluminate rings in which octahedral aluminum centers are bridged with bis(μ_2-hydroxo) groups. Such complexes are immediately recognized as precursors for the formation of structures such as gibbsite ($Al(OH)_3$), whose basic unit is the Al_6 ring. We also observed larger complexes such as Al_9, Al_{10}, Al_{12} containing Al_6 ring units, and Al_{13} (Keggin ion). In a further confirmation of our results, a Al_{13}^{2+} Keggin ion[49] was also observed previously. Complexation between aluminum and perchlorate ($-OClO_3$) species was evident from the chlorine isotopic peak separations. The species contain various numbers of $-OClO_3$ ions. Although the Al_6 ring motif is always present, there are clearly several isomeric arrangements of perchlorate anions, hydroxyl groups, and water molecules on the edges of these complexes. The structures shown in Figure 9 depict only individual isomers of these species.

dx.doi.org/10.1021/ja111055q | J. Am. Chem. Soc. 2011, 133, 5397–5412

Table 2. Silicate Complexes Identified from Positive and Negative Charge Scan Modes of ESI-MS (m/z 20−900) in Mildly Acidic Solutions (pH ~3.2) after 1 h of Hydrolysis of TEOS at 25 °C

chemical formula of Si species detected at 25 °C [ESI(+)]	peak (m/z)
$[Si_2O(OH)_5(H_2O)]^+$	175
$[Si_3O_3(OH)_5(H_2O)]^+$	235
$[Si_4O_6(OH)_3(H_2O)]^+$	277
$[Si_5O_6(OH)_7(H_2O)]^+$	373
$[Si_6O_9(OH)_5(H_2O)]^+$	415
$[Si_7O_{10}(OH)_7(H_2O)]^+$	493
$[Si_8O_{12}(OH)_7(H_2O)]^+$	553
chemical formula of species detected at 25 °C [ESI(−)]	**peak series (m/z)**
$[Cl(O)_{n+3}]^-$	$83 + 16n$ ($n = 0-1$)

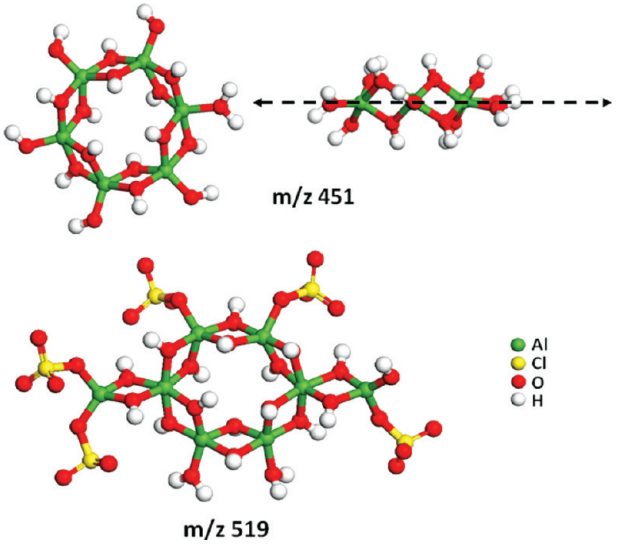

Figure 9. DFT-optimized geometries of selected planar complexes identified in a mildly acidic aqueous aluminate solution at 25 °C. The upper structure (Al_6) with m/z = 451 is shown in two orientations: top view (left) and side view (right). As indicated by the dashed line, the complex is planar. See Supporting Information Figure S13 for labeled 3D and uncolored 2D ChemDraw versions of these structures.

These structures are clearly shown to have planar minimum-energy configurations by the DFT calculations. On the basis of our overall observations of the structural patterns in the identified monomer and dimer complexes, we find that variations in the number of attached perchlorate ions are primarily caused by the replacement of outer −OH groups with $-OClO_3$ groups. Bidentate ($=O_2ClO_2$) complexation of perchlorate anions with aluminates can potentially also occur. However, our quantitative analysis of the low-molecular-weight species clearly indicated that the molecular formulas are only consistent with monodentate complexation in the form of $-OClO_3$. A very recent ESI study on aluminum speciation in aqueous $AlCl_3$ solutions containing the ClO_4^- anion has suggested that the perchlorate anion might also help bridge two aluminum ions.[50] Other recent findings indicated denser, "brucite-like" aluminate complexes in hydrolyzed aluminum

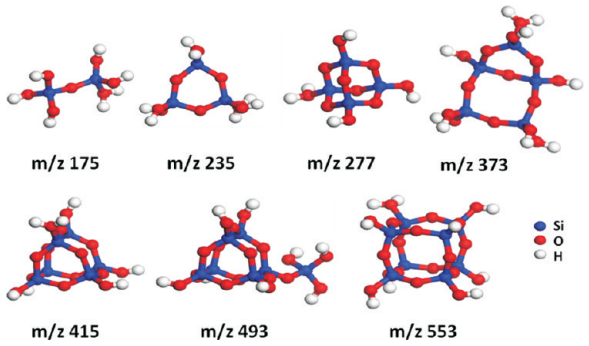

Figure 10. DFT-optimized geometries of selected complexes identified in a mildly acidic aqueous silicate solution at 25 °C. See Supporting Information Figure S13 for labeled 3D and uncolored 2D ChemDraw structures.

solutions that did not contain perchlorate ions,[29,53] whereas our results clearly indicate species with a gibbsite (six-membered ring) structure (m/z = 519 in Figure 9) and also confirm previous SAXS studies.[27] The observed complexation of perchlorate ions with almost all the aluminate species (Table 1) may indicate their role in stabilizing species whose basic unit is the six-membered gibbsite ring and inhibiting formation of brucite-like clusters. The complexation of aluminate species by perchlorate anions may also prevent further condensation of species larger than Al_{13}. Therefore, we believe that complexation of aluminosilicate species with perchlorate anions is important in understanding the mechanism of nanotube formation. We did not detect species larger than Al_{13}, but previous studies on aluminate solutions indicated the possible existence of Al_{30}[28] and Al_{26}[54] structures that might be formed by condensation of more than one Keggin unit.

Next, we studied silicon speciation in mildly acidic solutions by ESI-MS(+) and ESI-MS(−) after 1 h of hydrolysis of TEOS at 25 °C. Distances between the isotopic patterns (^{28}Si, ^{29}Si) are observed to be 1 m/z, showing that the species have 1 unit of charge. Hydrolysis of TEOS predominantly resulted in the formation of small silicate species such as the dimer (m/z = 175) and cyclic trimer (m/z = 235).[55] The silicate monomer was not detected in either scan mode. Complete hydrolysis occurred, and no ethoxy ($-OC_2H_5$) ligands were detected in the structures. Tetramer and pentamer silica species were also found at m/z = 277 and 373, respectively. The solution also contains cage-like polymeric ions. Signals at m/z = 415 and 533 were assigned to T6 and T8 cages, respectively. Previous studies also reported cage structures of silicates.[46,56] No complexation with perchlorate anions (ClO^-_4) was detected. As expected, no silicon species were detected in the negative scan mode. Figure 10 shows DFT-optimized geometries of the species identified in the silicate solution, which are predominantly cyclic in structure. Previous computational works using DFT and free energy calculations[56,57] also reported that cyclic silicate species are very stable and highly likely to be formed.

Aluminosilicate Speciation in Nanotube Synthesis Solutions. Having confirmed the reliability of our ESI-MS measurements and analysis techniques, we then obtained ESI-MS spectra from nanotube synthesis solutions at various stages. The spectra collected throughout the aging stage did not show significant differences in peak positions. Therefore, we conclude that the main species in the synthesis solution do not change during the aging stage. Figure S7 in the Supporting Information shows an

Table 3. Aluminosilicate Complexes Identified from Positive and Negative Charge Scan Modes of ESI-MS (m/z 20−900) in the Nanotube Synthesis Solution after 1 h of Aging at 25 °C

chemical formulas of species detected during aging at 25 °C	peak series (m/z)
ESI(+)	
$[Al(OH)_2(H_2O)_n]^+$	$61 + 18n$ ($n = 0-2$)
$[Al(OH)(H_2O)_n(ClO_4)]^+$	$143 + 18n$ ($n = 0-3$)
$[Al(H_2O)_n(ClO_4)_2]^+$	$225 + 18n$ ($n = 0-3$)
$[Al_2(OH)_4(H_2O)_n(ClO_4)]^+/[AlSiO(OH)_3(H_2O)_n(ClO_4)]^+$	$221 + 18n$ ($n = 0-3$)
$[Al_2SiO_2(OH)_5(H_2O)_{n+1}]^+/[Al_3O(OH)_6(H_2O)_{n+1}]^+$	$217 + 18n$ ($n = 0-3$)
$[Al_3SiO_2(OH)_6(H_2O)_n(ClO_4)]^{2+}$	$171 + 9n$ ($n = 0-5$)
$[Al_3SiO_2(OH)_8(H_2O)_n]^+/m/z$ 277: $[Si_4O_6(OH)_3(H_2O)]^+$	$277 + 18n$ ($n = 0-2$)
$[Al_7Si_2O_5(OH)_{13}(H_2O)_{n+3}(ClO_4)_3]^{3+}$	$299 + 6n$ ($n = 0-4$)
$[Al_2(OH)_3(H_2O)_n(ClO_4)_2]^+$	$303 + 18n$ ($n = 0-5$)
$[Al_7Si_2O_5(OH)_{12}(H_2O)_n(Cl^{35}O_4)_3(Cl^{37}O_4)]^{3+}$	$309 + 6n$ ($n = 0-10$)
$[Al_8Si_2O_6(OH)_{13}(H_2O)_n(Cl^{35}O_4)_3(Cl^{37}O_4)]^{3+}$	$329 + 6n$ ($n = 0-7$)
$[Al_2(OH)_2(H_2O)_n(ClO_4)_3]^+$	$385 + 18n$ ($n = 0-4$)
$[Al_2(OH)_2(H_2O)_n(Cl^{35}O_4)_2(Cl^{37}O_4)]^+$	$387 + 18n$ ($n = 0-4$)
$[Al_2SiO(OH)_5(H_2O)_n(ClO_4)_2]^+$	$381 + 18n$ ($n = 0-3$)
$[Al_4SiO_3(OH)_8(H_2O)_{n+1}(ClO_4)]^+$	$437 + 18n$ ($n = 0-2$)
$[Al_2SiO(OH)_4(H_2O)_n(ClO_4)_3]^+$	$463 + 18n$ ($n = 0-4$)
$[Al_5SiO_3(OH)_{12}(H_2O)_{n+1}]^+/[Al_4Si_2O_4(OH)_{11}(H_2O)_{n+1}]^+$	$433 + 18n$ ($n = 0-6$)
$[Al_5Si_2O_5(OH)_{12}(H_2O)_{n+1}]^+$	$493 + 18n$ ($n = 0-3$)
$[Al_6SiO_3(OH)_{15}(H_2O)_n]^+$	$493 + 18n$ ($n = 0-3$)
$[Al_4Si_2O_4(OH)_{10}(H_2O)_n(ClO_4)]^+/[Al_5SiO_3(OH)_{11}(H_2O)_n(ClO_4)]^+$	$497 + 18n$ ($n = 0-4$)
$[Al_{10}SiO_3(OH)_{22}(H_2O)_n(ClO_4)_3(ClO_4)]^{2+}$	$559 + 9n$ ($n = 0-4$)
$[Al_8Si_2O_5(OH)_{15}(H_2O)_{n+5}(Cl^{35}O_4)_4(Cl^{37}O_4)]^{2+}$	$597 + 9n$ ($n = 0-4$)
$[Al_{10}Si_3O_9(OH)_{18}(H_2O)_{n+1}(Cl^{35}O_4)_3(Cl^{37}O_4)]^{2+}$	$610 + 9n$ ($n = 0-5$)
$[Al_{12}Si_3O_9(OH)_{27}(H_2O)_{n+6}(Cl^{35}O_4)]^{2+}$	$609 + 9n$ ($n = 0-4$)
$[Al_{12}Si_3O_9(OH)_{25}(H_2O)_n(Cl^{35}O_4)_2(Cl^{37}O_4)]^{2+}$	$638 + 9n$ ($n = 0-6$)
$[Al_{13}Si_2O_{10}(OH)_{22}(H_2O)_{n+1}(Cl^{35}O_4)_2(Cl^{37}O_4)]^{2+}$	$638 + 9n$ ($n = 0-6$)
$[Al_{12}Si_3O_9(OH)_{26}(H_2O)_{n+1}(ClO_4)_2]^{2+}$	$605 + 9n$ ($n = 0-7$)
$[Al_{12}Si_5O_{12}(OH)_{29}(H_2O)_{n+3}(ClO_4)]^{2+}$	$678 + 9n$ ($n = 0-4$)
$[Al_{13}O_4(OH)_{24}(H_2O)_{n+2}(Cl^{35}O_4)_4(Cl^{37}O_4)]^{2+}$	$678 + 9n$ ($n = 0-4$)
$[Al_{12}Si_4O_{10}(OH)_{29}(H_2O)_{n+6}(Cl^{35}O_4)]^{2+}$	$648 + 9n$ ($n = 0-4$)
$[Al_{12}Si_7O_{16}(OH)_{30}(H_2O)_{n+5}]^{2+}$	$688 + 9n$ ($n = 0-5$)
$[Al_{12}Si_4O_{10}(OH)_{28}(H_2O)_{n+8}(Cl^{35}O_4)_2]^{2+}$	$707 + 9n$ ($n = 0-4$)
$[Al_{13}Si_4O_{16}(OH)_{18}(H_2O)_{n+5}(Cl^{35}O_4)_2(Cl^{37}O_4)]^{2+}$	$707 + 9n$ ($n = 0-4$)
$[Al_{12}Si_7O_{13}(OH)_{35}(H_2O)_{n+5}(ClO_4)]^{2+}$	$756 + 9n$ ($n = 0-3$)
$[Al_{13}Si_6O_{10}(OH)_{40}(H_2O)_{n+3}(ClO_4)]^{2+}$	$756 + 9n$ ($n = 0-3$)
ESI(−)	
$[Cl(O)_{n+3}]^-$	$83 + 16n$ ($n = 0-1$)
$[Al(OH)(ClO_4)_3]^-$	m/z 341
$[Al(ClO_4)_4]^-$	m/z 425
$[Al_3O_3(OH)(H_2O)_n(ClO_4)_3]^-$	$443 + 18n$ ($n = 0-3$)
$[Al_2SiO_2(OH)_4(H_2O)_3(ClO_4)_3]^-/[Al_3O(OH)_5(H_2O)_3(ClO_4)_3]^-$	m/z 533
$[Al_4Si_2O_4(OH)_{12}(H_2O)_{n+2}(ClO_4)]^-$	$567 + 18n$ ($n = 0-1$)

ESI-MS spectra of the nanotube synthesis solution (taken after 1 h of aging at 25 °C), and Table 3 shows the chemical composition of species identified by our exhaustive quantitative procedure. It is clear that the nanotube synthesis is controlled by aluminate speciation. No signals from silicate species were detected. As in the pure aluminate solution, the distribution of aluminosilicate species in solution ranged from having 1−13 aluminum atoms in their structures, the differences being only in the number of attached silicon tetrahedra and perchlorate anions (i.e., $Al_1Si_x(ClO_4)_y$−$Al_{13}Si_x(ClO_4)_y$). Keggin ions with attached silicate groups were also identified.

There are several important points to be highlighted at this stage. First, it is significant that nearly all species could be explained with the same basic structural characteristics as found in the aluminate solution, such as the octahedral aluminum units linked by μ_2-OH groups at shared edges, the existence of aluminosilicate gibbsite-like units with a Q^3(6Al) configuration of Si, the binding of perchlorate ions to the edges of the

dx.doi.org/10.1021/ja111055q | J. Am. Chem. Soc. 2011, 133, 5397–5412

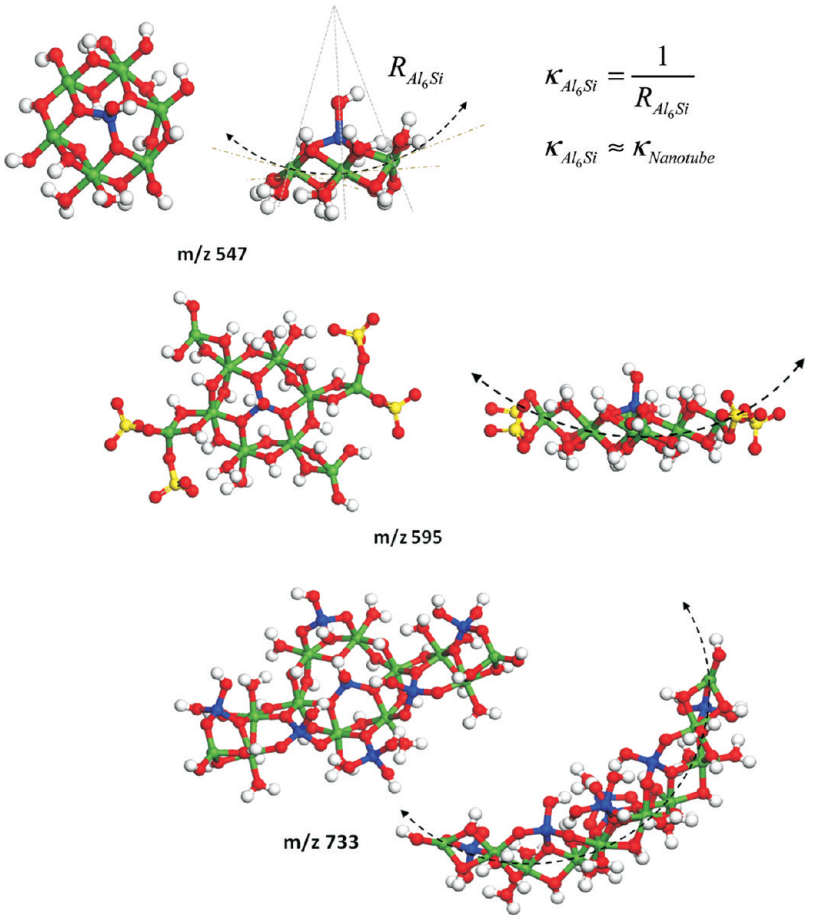

Figure 11. DFT-optimized geometries of selected aluminosilicate proto-nanotube precursors identified by ESI-MS. The species m/z = 547, 595, and 733 are shown in two orientations: top view (left) and side view (right). Dotted circles show example locations of Al tetrahedra adjoined by Si atoms in Si(nAl) coordination. The dashed lines follow the inherent curvature (κ) of these species, as measured from their radii of curvature (R). As shown, $\kappa_{Al_6Si} \approx \kappa_{Al_{12}Si_7} \approx \kappa_{nanotube}$. See Supporting Information Figure S13 for labeled 3D and uncolored 2D ChemDraw versions of these structures.

aluminosilicate complexes, and the existence of end-groups consisting of highly distorted tetra-coordinated aluminum sites (with Al−OH or Al−$OClO_3$ bonds). The silicate species are attached to aluminate complexes that are already in a nanotube-like configuration, most notably the Al_6 rings with silicon attached in a Q^3(6Al) configuration as well as larger sheet-like structures in which this structural motif is repeated. These complexes constitute the first direct evidence of "proto-nanotube" species existing in the solution. Second, these ESI-MS findings are directly supported by our NMR results. Third, the aluminosilicate, aluminate, and silicate speciation arises naturally from the arithmetic analysis of the ESI-MS data and does not involve any structural assumptions other than the list of elements, isotopes, ligands, and reasonably expected coordination environments (e.g., octahedral Al, tetrahedral Al and Si). Fourth, the conversion of tetrahedral aluminum to octahedral aluminum was proposed as being necessary prior to proto-imogolite formation[13] and was interpreted as being a result of silicate species bridging two aluminate species. On the other hand, it appears here that such a conversion more likely occurs due to rearrangement of tetrahedral aluminum (found on the edges of the proto-nanotube sheets) into octahedral aluminum during the assembly of the nanotube, by condensation of these proto-nanotube complexes.

Solvated DFT-based geometry optimizations performed on selected key species revealed the *inherent curvature* of identified aluminosilicate precursors (Figure 11) in comparison to the *planar* precursors found in aluminate solutions (Figure 9). The precursor with m/z = 547 consists of a hexagonal ring of aluminate octahedra and tetrahedra, with a silanol group attached to it. This structure is closely related to the structure of the final nanotube material, and its radius of curvature is almost identical to that of the final nanotube material. Larger precursors such as m/z = 595 and 733 also show the existence of the same structural motif as the precursor with m/z = 547. The present study therefore indicates the potential for engineering the curvature of nanostructured materials (such as nanotubes and nanoshells) by controlling the speciation of the molecular and nanoscale precursors.

The species identified in the subsequent heating step at 95 °C are listed in Table 4. Upon heating the aged solution to 95 °C to induce nanotube assembly, it is observed that all proto-nanotube species in the m/z 500−800 region of the ESI-MS spectra disappear within 3 h, but the species identified in the m/z 50−500 region remain nearly constant throughout the reaction (Supporting Information Figures S8 and S9). This is consistent with the condensation of the proto-nanotube precursors into larger nanoparticles which then rearrange into

Table 4. Aluminosilicate Complexes Identified from Positive and Negative Charge Scan Modes of ESI-MS (m/z 20−900) in the Nanotube Synthesis Solution during the Heating Stage at 95 °C

chemical formula of species detected during heating at 95 °C	peak series (m/z)
ESI(+)	
$[Al(OH)_2(H_2O)_n]^+$	$61 + 18n$ (n = 0−2)
$[Al(OH)(H_2O)_n(ClO_4)]^+$	$143 + 18n$ (n = 0−3)
$[Al(H_2O)_n(ClO_4)_2]^+$	$225 + 18n$ (n = 0−3)
$[Al_2(OH)_4(H_2O)_n(ClO_4)]^+/[AlSiO(OH)_3(H_2O)_n(ClO_4)]^+$	$221 + 18n$ (n = 0−3)
$[Al_2SiO_2(OH)_5(H_2O)_{n+1}]^+/[Al_3O(OH)_6(H_2O)_{n+1}]^+$	$217 + 18n$ (n = 0−3)
$[Al_3SiO_2(OH)_6(H_2O)_n(ClO_4)]^{2+}$	$171 + 9n$ (n = 0−5)
$[Al_3SiO_2(OH)_8(H_2O)_n]^+$/$m/z$ 277: $[Si_4O_6(OH)_3(H_2O)]^+$	$277 + 18n$ (n = 0−2)
$[Al_7Si_2O_5(OH)_{13}(H_2O)_{n+3}(ClO_4)_3]^{3+}$	$299 + 6n$ (n = 0−4)
$[Al_2(OH)_3(H_2O)_n(ClO_4)_2]^+$	$303 + 18n$ (n = 0−5)
$[Al_7Si_2O_5(OH)_{12}(H_2O)_n(Cl^{35}O_4)_3(Cl^{37}O_4)]^{3+}$	$309 + 6n$ (n = 0−10)
$[Al_8Si_2O_6(OH)_{13}(H_2O)_n(Cl^{35}O_4)_3(Cl^{37}O_4)]^{3+}$	$329 + 6n$ (n = 0−7)
$[Al_2(OH)_2(H_2O)_n(ClO_4)_3]^+$	$385 + 18n$ (n = 0−4)
$[Al_2(OH)_2(H_2O)_n(Cl^{35}O_4)_2(Cl^{37}O_4)]^+$	$387 + 18n$ (n = 0−4)
$[Al_2SiO(OH)_5(H_2O)_n(ClO_4)_2]^+$	$381 + 18n$ (n = 0−3)
$[Al_4SiO_3(OH)_8(H_2O)_{n+1}(ClO_4)]^+$	$437 + 18n$ (n = 0−2)
$[Al_2SiO(OH)_4(H_2O)_n(ClO_4)_3]^+$	$463 + 18n$ (n = 0−4)
$[Al_5SiO_3(OH)_{12}(H_2O)_{n+1}]^+/[Al_4Si_2O_4(OH)_{11}(H_2O)_{n+1}]^+$	$433 + 18n$ (n = 0−6)
$[Al_5Si_2O_5(OH)_{12}(H_2O)_{n+1}]^+$	$493 + 18n$ (n = 0−3)
$[Al_6SiO_3(OH)_{15}(H_2O)_n]^+$	$493 + 18n$ (n = 0−3)
$[Al_4Si_2O_4(OH)_{10}(H_2O)_n(ClO_4)]^+/[Al_5SiO_3(OH)_{11}(H_2O)_n(ClO_4)]^+$	$497 + 18n$ (n = 0−4)
$\mathbf{[Al_3SiO_2(OH)_7(H_2O)_{n+6}]^{2+}}$	$\mathbf{184 + 9n}$ **(n = 0−1)**
$\mathbf{[Al_3SiO_2(OH)_5(H_2O)_{n+6}(ClO_4)_2]^{2+}}$	$\mathbf{266 + 9n}$ **(n = 0−1)**
$\mathbf{[Al_3SiO_2(OH)_8(H_2O)_{n+2}]^+}$	$\mathbf{313 + 18n}$ **(n = 0−2)**
ESI(−)	
$[Cl(O)_{n+3}]^-$	$83 + 16n$ (n = 0−1)
$[Al(OH)(ClO_4)_3]^-$	m/z 341
$[Al(ClO_4)_4]^-$	m/z 425
$[Al_3O_3(OH)(H_2O)_n(ClO_4)_3]^-$	$443 + 18n$ (n = 0−4)
$[Al_2SiO_2(OH)_4(H_2O)_3(ClO_4)_3]^+/[Al_3O(OH)_5(H_2O)_3(ClO_4)_3]^+$	m/z 533

short nanotubes, a mechanism proposed by us previously.[14] New Al_3Si species, highlighted in bold in Table 4, appeared within 24 h of heating. We therefore tentatively assign the new 3−5 ppm peak appearing in the ^{27}Al NMR spectra to these Al_3Si species.

Dynamic Light Scattering. We used DLS measurements as a function of aging and reaction time of aluminosilicate nanotube synthesis solutions to reveal the change in average particle size together with semiquantitative measurements of total particle concentration throughout the nanotube synthesis. Details of quantitative DLS analysis of nanotube solutions can be found elsewhere[2] (also see Supporting Information Figure S10).

Figure 12a shows the average particle size as a function of synthesis time. We observed particles with a Stokes−Einstein hydrodynamic diameter of 200−220 nm during the aging stage. The polydispersity of the particles was quite low and did not vary significantly with aging time. These particles are X-ray amorphous, and no nanotubes are formed during the aging step. As shown in Supporting Information Figure S11, two dynamical processes were observed in the initial 3 h of heating, but they were reduced to a single process subsequently. A two-exponential autocorrelation decay function was used to fit the data and to extract diffusion coefficients:[2,58]

$$g_2(t) = 1 + \beta\left|A_1\, e^{-D_2 q^2 \tau} + A_2\, e^{-D_2 q^2 \tau}\right|^2$$

Here, β is the coherence factor, which can be taken as unity in dilute aqueous suspensions, and the scattering vector $q = (4\pi n/\lambda)\sin(\theta/2)$, where n is the refractive index of water, λ is the wavelength of the incident light, and θ is the scattering angle. A_1 and A_2 are the amplitudes of fast and slow relaxation modes, respectively. A_2 is found to be zero except for the first 3 h of heating.

After 1 h of reaction time, the diffusion coefficient D_1 (fast dynamics) is 3.8×10^{-7} cm^2/s, whereas D_2 (slow dynamics) is found to be 8.0×10^{-11} cm^2/s. The value of D_1 is close to the diffusion coefficient reported for short (∼20 nm length) aluminogermanate nanotubes.[2] This dynamics corresponds to the diffusion of short aluminosilicate proto-nanotubes with length ∼10 nm. We attribute the second, slow diffusion coefficient to the formation (immediately upon heating) of a loosely connected, gel-like network of partially condensed aluminosilicate precursors. Such structures have also previously been observed

dx.doi.org/10.1021/ja111055q | J. Am. Chem. Soc. 2011, 133, 5397–5412

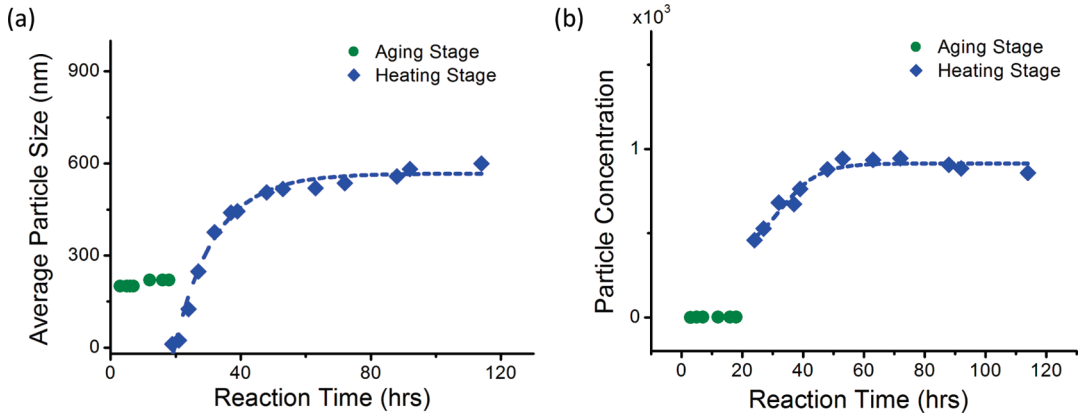

Figure 12. (a) Average particle diameter (during aging at 25 °C) and nanotube length (during heating at 95 °C) and (b) particle (or nanotube) concentration obtained from normalized DLS intensity by unit particle volume and precursor concentration as functions of reaction time.

by DLS in clay systems.[59] Furthermore, the effective Stokes−Einstein hydrodynamic diameter corresponding to the slow dynamical process is very large (~20 μm), clearly indicating that it cannot correspond to individual particles dispersed in the solution. After 3 h of reaction at 95 °C, the values of D_1 and D_2 are 1.8×10^{-7} and 5.0×10^{11} cm^2/s, respectively. The average nanotube length continues to increase with reaction time and reaches a plateau after 24 h, as also observed previously by TEM studies.[19] This observation indicates that, during the first 24 h, fast molecular rearrangement of existing precursor species into nanotubes takes place. Such molecular rearrangements are also evident from our detailed ^{27}Al liquid-state NMR data and tracking of individual resonances throughout the reaction time (96 h), as shown in Figure 4f,g and Supporting Information Figure S3a−c. Within 24 h, the NMR chemical shift of the 6 ppm peak (assigned to species with Q^3(6Al) configuration) reaches that of the purified nanotubes. However, the changes in the chemical shift of the 6 ppm peak are very minor (only 0.4 ppm over 96 h). This indicates the occurrence of only slight structural changes, such as those occurring in a rearrangement and condensation of already existing molecular precursors. On the other hand, more substantial changes in the NMR chemical shift (~3 ppm) occur during aging, signifying the evolution in precursor structure.

The light scattering intensity, when normalized by the particle volume and precursor concentration, can provide semiquantitative information on the total particle concentration,[60] as shown in Figure 12b. The ~200 nm particle concentration slightly increases upon aging (Supporting Information Figure S12). This observation shows a resemblance to the behavior of ^{27}Al liquid-state NMR resonances near 6 ppm and the Keggin ion signal during aging, as shown in Figure 4c,d and Supporting Information Figure S2f. We were not able to detect these large particles by ESI-MS. Hence, their exact chemical composition is not clear. However, it is clear from Figure 12b that the concentration of the ~200 nm particles formed during aging is very small compared to the precursor and nanotube concentrations. Therefore, these particles cannot be directly responsible for the formation of nanotubes.

Overall Mechanism of Nanotube Formation. On the basis of the detailed insights from ESI-MS and NMR investigations, we construct a molecular-level mechanism of single-walled aluminosilicate nanotube formation (Figure 13). Stable proto-nanotube intermediates with intrinsic curvature form within 1 h of aging and remain essentially unchanged throughout this step. Within 7 h of the initial mixing of reactants, a dynamic equilibrium between "small", "medium", and "large" aluminosilicate precursors is established.

We depict the equilibria involving some main species detected by ESI-MS as follows:

$$2\left[Al_2SiO_2(OH)_5(H_2O)\right]^+ \leftrightarrow \left[Al_4Si_2O_4(OH)_{11}(H_2O)\right]^{2+} + [H]^+$$

$$3\left[Al_4SiO_3(OH)_8(H_2O)(ClO_4)\right]^+ \leftrightarrow \left[Al_{12}Si_3O_9(OH)_{26}(H_2O)(ClO_4)_2\right]^{2+} + 2[H]^+ + ClO_4^-$$

$$\left[Al_{12}Si_4O_{10}(OH)_{28}(H_2O)_8(ClO_4)_2\right]^{2+} + \left[Al(ClO_4)_4\right] \leftrightarrow \left[Al_{13}Si_4O_{16}(OH)_{18}(H_2O)_5(ClO_4)_3\right]^{2+} + 2[H]^+ + ClO_4^- + 7H_2O$$

The experimental findings that support such equilibria are summarized as follows: (1) there is a slight decrease in pH from 3.7 to 3.3 during aging; (2) there is an increase in the integrated area of Keggin peaks at 63.3 ppm, 12 ppm, and 6 ppm peak in liquid-state ^{27}Al NMR that represents species in nanotube-like configuration; (3) there is a decrease in line width and chemical shift of the 6 ppm peak in liquid-state ^{27}Al NMR; (4) there is slight decrease in area % of −90 ppm peak in ^{29}Si MAS NMR spectra as a function of aging time; (5) we find a decrease in the detected amount of tetra-coordinated Al as a function of aging time by solid-state ^{27}Al NMR; and (6) ESI-MS showed that main species remained essentially similar throughout the aging, but NMR peaks showed minor changes in terms of their chemical shift, integrated area, and fwhm values.

The DFT simulations revealed that the Al_6Si_x−$Al_{12}Si_x$ aluminosilicate species have intrinsically curved structures, in contrast to the planar structures observed in the aluminate solutions. Upon heating the aged nanotube synthesis solution, the nanoscale aluminosilicate intermediate species represented by the ESI-MS region m/z 500−800 (i.e., Al_8Si_x−$Al_{13}Si_x$) disappear from the ESI-MS spectra. Those species are hence condensing into larger nanoparticle aggregates, as observed by DLS, and then rearranging into the initial nanotubes and subsequently growing by a variety of processes (e.g., precursor attachment, end-to-end

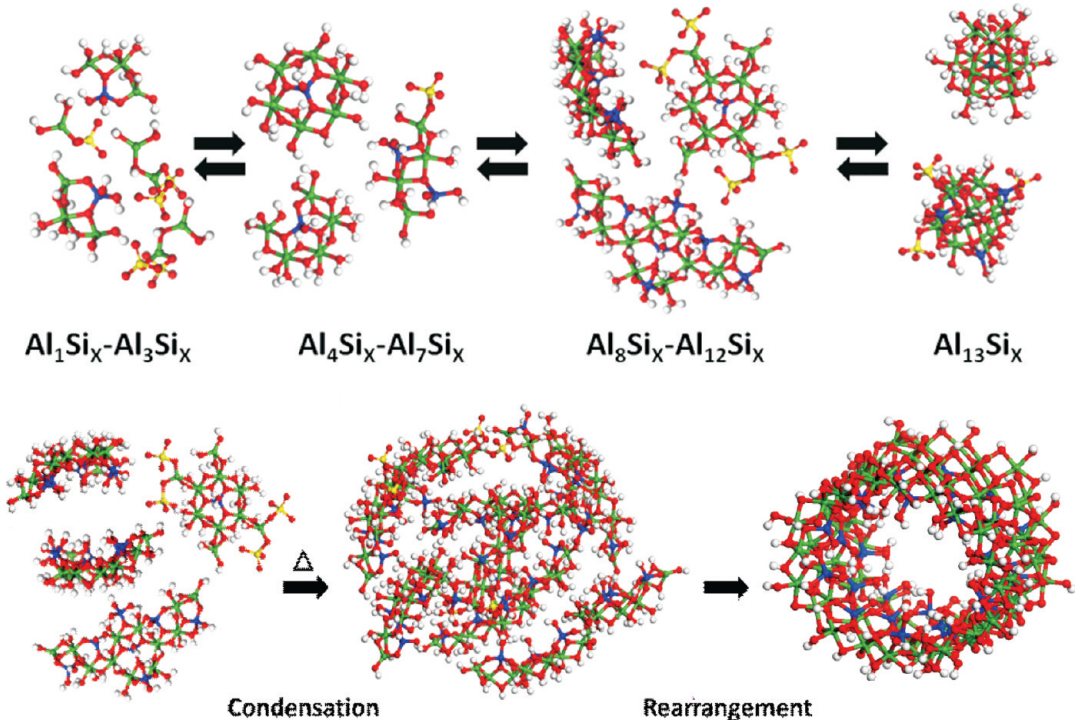

Figure 13. Formation mechanism of aluminosilicate nanotubes. (Top) Equilibrium established between aluminosilicate species during the aging stage at 25 °C. (Bottom) Condensation and rearrangement of Al_8Si_x−$Al_{12}Si_x$ species upon heating. Also see Supporting Information Figure S13 for labeled 3D and uncolored 2D ChemDraw structures.

aggregation). Our experimental findings that support such a mechanism are summarized as follows: (1) an abrupt decrease in pH immediately upon heating to 95 °C and nearly constant pH throughout the remaining 95 h of reaction; (2) nearly constant area of liquid-state ^{27}Al NMR 6 ppm peak that represents the nanotube-like aluminum bonding environment; (3) disappearance of tetra-coordinated aluminum species within a few hours of heating; (4) rearrangement detected by increase in area % of −80 ppm and decrease in −90 ppm peak in solid-state ^{29}Si NMR; and (5) again rearrangement detected by increase in area % of Al(VI)a arrangement and decrease in area % of Al(VI)c coordination environment.

The role of the aluminosilicate Keggin-like ions remains unclear. The literature on aluminate solutions suggests the transformation of aluminate Keggin ions into planar gibbsite-like layered structures. We did not observe such a rearrangement in the aluminosilicate solution. In contrast, the aluminosilicate solution contains a richer variety of species, many of which are complexed with perchlorate ions. On the basis of our observations as discussed above, we cannot distinguish whether the $Al_{13}Si_x$ Keggin species participate in the condensation and rearrangement of the nanoscale species into nanotubes, or whether they decompose into smaller species such as the Al_3Si_x units that appear upon heating the nanotube synthesis solution.

■ CONCLUSION

A detailed molecular-level account of the formation mechanism of single-walled aluminosilicate nanotubes has been given via combined ESI-MS and NMR characterization. It provides, for the first time, a clear understanding of the main speciation and nanotube assembly processes. ESI-MS is shown to be an excellent tool for analysis of the precursor species in nanotube synthesis solutions. This paper clarifies the structure of nanotube-like precursors, including the proposed sheet-like precursor called proto-imogolite. Geometry optimization of the structures of these precursors, which are formed at an early stage after initial hydrolysis of the reactants, reveal that they possess inherent curvature. Therefore, we have shown that nanotube assembly is preceded by the formation of precursors that already possess a similar chemical coordination environment of the Al and Si atoms, as well as an inherent tendency to form curved nanostructures. The condensation of these proto-nanotube precursors into larger nanoparticles upon heating (as observed by DLS measurements and also by the disappearance of these species in ESI-MS spectra) provides a clear connection to the subsequent formation of ordered nanotubes. The rearrangement into nanotubes is accomplished by the conversion of tetra-coordinated end groups of these precursor species to a fully octahedral configuration as the precursors condense together. Anions in solution (particularly perchlorate) are found to initially complex the aluminosilicate precursors. Understanding in more detail the role of these anions, as well as other possible ligands such as organic molecules and metal oxide species, may be important in controlling the nanotube structure and dimensions, and is a subject for further investigation. The molecular-level nanotube formation mechanism also provides a basis for investigations of the subsequent growth mechanisms at larger length scales, via techniques such as cryo-TEM and SAXS that can reveal the assembly and morphological evolution of the growing nanotubes. Overall, the insights obtained in this work, and following from it, provide a possible basis for engineering *curved nanoscale objects* (such as single-walled nanotubes, nanoshells, and nanospheres) with tunable shape, size, composition, and structure.

■ ASSOCIATED CONTENT

Supporting Information. Detailed NMR, ESI-MS, and DLS spectra; labeled structures of the main molecular species. This material is available free of charge via the Internet at http://pubs.acs.org.

■ AUTHOR INFORMATION

Corresponding Author
sankar.nair@chbe.gatech.edu

■ ACKNOWLEDGMENT

The authors acknowledge financial support of this work by NSF (CAREER, CBET-0846586) and DFG (SCHE 524/9). We also acknowledge D. Bostwick, Prof. F. Fernandez, D.-Y. Kang, and Dr. J. Leisen (Georgia Tech) for helpful discussions and assistance with nanotube synthesis and NMR and ESI-MS data collection.

■ REFERENCES

(1) Tenne, R.; Rao, C. N. R. *Philos. Trans. Math. Phys. Eng. Sci.* **2004**, *362*, 2099.
(2) Mukherjee, S.; Bartlow, V. M.; Nair, S. *Chem. Mater.* **2005**, *17*, 4900.
(3) Hu, S.; Ling, X.; Lan, T.; Wang, X. *Chem.—Eur. J.* **2010**, *16*, 1889.
(4) Imamura, S.; Kokubu, T.; Yamashita, T.; Okamoto, Y.; Kajiwara, K.; Kanai, H. *J. Catal.* **1996**, *160*, 137.
(5) Imamura, S.; Hayashi, Y.; Kajiwara, K.; Hoshino, H.; Kaito, C. *Ind. Eng. Chem. Res.* **1993**, *32*, 600.
(6) Zang, J.; Chempath, S.; Konduri, S.; Nair, S.; Sholl, D. S. *J. Phys. Chem. Lett.* **2010**, *1*, 1235.
(7) Ohashi, F.; Tomura, S.; Akaku, K.; Hayashi, S.; Wada, S. I. *J. Mater. Sci.* **2004**, *39*, 1799.
(8) Farmer, V. C.; Adams, M. J.; Fraser, A. R.; Palmieri, F. *Clay Miner.* **1983**, *18*, 459.
(9) Konduri, S.; Mukherjee, S.; Nair, S. *ACS Nano* **2007**, *1*, 393.
(10) Cradwick, C. P. G.; Farmer, V. C.; Russell, J. D.; Masson, C. R.; Wada, K.; Yoshinaga, N. *Nat. Phys. Sci.* **1972**, *240*, 187.
(11) Wada, S. I.; Wada, K. *Clays Clay Miner.* **1982**, *30*, 123.
(12) Farmer, V. C.; Fraser, A. R. *Int. Clay Conf.* **1979**, *27*, 547.
(13) Wilson, M. A.; Lee, G. S. H.; Taylor, R. C. *J. Non-Cryst. Solids* **2001**, *296*, 172.
(14) Mukherjee, S.; Kim, K.; Nair, S. *J. Am. Chem. Soc.* **2007**, *129*, 6820.
(15) Levard, C.; Rose, J.; Thill, A.; Masion, A.; Doelsch, E.; Maillet, P.; Spalla, O.; Olivi, L.; Cognigni, A.; Ziarelli, F.; Bottero, J. Y. *Chem. Mater.* **2010**, *22*, 2466.
(16) Kragten, D. D.; Fedeyko, J. M.; Sawant, K. R.; Rimer, J. D.; Vlachos, D. G.; Lobo, R. F.; Tsapatsis, M. *J. Phys. Chem. B* **2003**, *107*, 10006.
(17) Kirschhock, C. E. A.; Ravishankar, R.; Looveren, L. V.; Jacobs, P. A.; Martens, J. A. *J. Phys. Chem. B* **1999**, *103*, 4972.
(18) Davis, T. M.; Drews, T. O.; Ramanan, H.; He, C.; Dong, J.; Schnablegger, H.; Katsoulakis, M. A.; Kokkoli, E.; McCormick, A. V.; Penn, R. L.; Tsapatsis, M. *Nat. Mater.* **2006**, *5*, 400.
(19) Yang, H.; Wang, C.; Su, Z. *Chem. Mater.* **2008**, *20*, 4484.
(20) Zhao, Y.; Frost, R. L.; Martens, W. N.; Zhu, H. Y. *Langmuir* **2007**, *23*, 9850.
(21) Massiot, D.; Fayon, F.; Capron, M.; King, I.; Le Calvé, S.; Alonso, B.; Durand, J.-O.; Bujoli, B.; Gan, Z.; Hoatson, G. *Magn. Reson. Chem.* **2002**, *40*, 70.
(22) Sarpola, A.; Hietapelto, V.; Jalonen, J.; Jokela, J.; Laitinen, R. S. *Phys. Chem. Chem. Phys.* **2007**, *9*, 377.
(23) Öhman, L. O.; Edlund, U. In *Encyclopedia of Nuclear Magnetic Resonance*; Grant, D. M., Harris, R. K., Eds.; John Wiley & Sons: Chichester, UK, 1996; Vol. 2, p 742.
(24) Delak, K. M.; Farrar, T. C.; Sahai, N. *J. Non-Cryst. Solids* **2005**, *351*, 2244.
(25) Kloprogge, J. T.; Seykens, D.; Jansen, J. B. H.; Geus, J. W. *J. Non-Cryst. Solids* **1992**, *142*, 94.
(26) Akitt, J. W.; Farthing, A. *J. Chem. Soc., Dalton Trans.* **1981**, *7*, 1617.
(27) Singhal, A.; Keefer, K. D. *Mater. Res. Soc. Symp. Proc.* **1994**, *9*, 1973.
(28) Allouche, L.; Gérardin, C.; Loiseau, T.; Férey, G.; Taulelle, F. *Angew. Chem.* **2000**, *112*, 521.
(29) Casey, W. H. *Chem. Rev.* **2005**, *106*, 1.
(30) Vogels, R. J. M. J.; Kloprogge, J. T.; Buinin, P. A.; Seykens, D.; Jansen, J. B. H.; Geus, J. W. *J. Non-Cryst. Solids* **1995**, *191*, 38.
(31) Vogels, R. J. M. J.; Kloprogge, J. T.; Geus, J. W. *J. Colloid Interface Sci.* **2005**, *285*, 86.
(32) Akitt, J. W.; Farthing, A. *J. Chem. Soc., Dalton Trans.* **1981**, *7*, 1617.
(33) Akitt, J. W.; Farthing, A. *J. Chem. Soc., Dalton Trans.* **1981**, *7*, 1624.
(34) Farmer, V. C.; Fraser, A. R.; Tait, J. M. *Geochim. Cosmochim. Acta* **1979**, *43*, 1417.
(35) Man, P. P. In *Encyclopedia of Nuclear Magnetic Resonance*; Grant, D. M., Harris, R. K., Eds.; John Wiley & Sons: Chichester, U.K., 1996, Vol. 6, p 3869.
(36) Bureau, B.; Silly, G.; Buzare, J. Y.; Boulard, B.; Legein, C. *J. Phys.: Condens. Matter* **2000**, *12*, 5775.
(37) Cornier, L.; Neuville, D. R.; Massiot, D. *Geochim. Cosmochim. Acta* **2004**, *68*, A650.
(38) Neuville, D. R.; Cormier, L.; Massiot, D. *Chem. Geol.* **2006**, *229*, 173.
(39) Vyalikh, A.; Massiot, D.; Scheler, U. *Solid State Nucl. Magn. Reson.* **2009**, *36*, 19.
(40) d'Espinose de Lacaillerie, J.-B.; Fretigny, C.; Massiot, D. *J. Magn. Reson.* **2008**, *192*, 244.
(41) Barron, P. F.; Wilson, M. A.; Campbell, A. S.; Frost, R. L. *Nature* **1982**, *299*, 616.
(42) Mackenzie, K. J. D.; Bowden, M. E.; Meinhold, R. H *Clays Clay Miner.* **1991**, *39*, 337.
(43) Corbin, D. R.; Burgess, B. F.; Vega, A. J.; Farlee, R. D. *Anal. Chem.* **1987**, *59*, 2722.
(44) Kim, Y.; Lee, S. K.; Kirkpatrick, R. J. *Am. Mineral.* **2010**, *95*, 1694.
(45) Neuhoff, P. S.; Stebbins, J. F.; Bird, D. K. *Am. Mineral.* **2003**, *88*, 410.
(46) Arago, J.; Vicent, C.; Julian, B.; Cordoncillo, E.; Escribano, P. *New J. Chem.* **2009**, *33*, 1100.
(47) Eberlin, M. N. *J. Mass. Spectrom.* **2007**, *13*, 19.
(48) Urabe, T.; Tsugoshi, T.; Tanaka, M.; Kumakura, S. *J. Mass Spectrom.* **2007**, *42*, 591.
(49) Urabe, T.; Tsugoshi, T.; Tanaka, M. *J. Mol. Liq.* **2008**, *143*, 70.
(50) Urabe, T.; Tsugoshi, T.; Tanaka, M. *J. Mass Spectrom.* **2009**, *44*, 193.
(51) Bussian, P.; Sobott, F.; Brutschy, B.; Schrader, W.; Schüth, F. *Angew .Chem.* **2000**, *39*, 3901.
(52) Sarpola, A.; Hietapelto, V.; Jalonen, J.; Jokela, J.; Laitinen, R. S. *J. Mass Spectrom.* **2004**, *39*, 423.
(53) Lin, Y.-F.; Lee, D.-J. *J. Phys. Chem. A* **2010**, *114*, 3503.
(54) Sarpola, A.; Hietapelto, V.; Jalonen, J.; Jokela, J.; Laitinen, R. S. *Int. J. Environ. Anal. Chem.* **2006**, *86*, 1007.
(55) Simonsen, M. E.; Søgaard, E. G. *Int. J. Mass Spectrom.* **2009**, *285*, 78.
(56) Pereira, J. C. G.; Catlow, C. R. A.; Price, G. D. *J. Phys. Chem. A* **1999**, *103*, 3252.
(57) Caratzoulas, S.; Vlachos, D. G.; Tsapatsis, M. *J. Am. Chem. Soc.* **2006**, *128*, 16138.
(58) Ivanov, D. A.; Winkelmann, J. *J. Chem. Phys.* **2006**, *125*, 104507.
(59) Marques, F. A. M. Master's Thesis, The Sapienza University of Rome, June 2007.
(60) Philo, S. J. *AAPS J.* **2006**, *8*, E564.